UNIVERSIDAD DE INVESTIGACIÓN DE TECNOLOGÍA EXPERIMENTAL YACHAY TECH

Escuela de Ciencias Químicas e Ingeniería

TÍTULO: "The Unusual Behavior of Galactose-Steroid Bingel-Hirsch Reaction for Functionalization of C_{60}-fullerene: A Theoretical Study".

Trabajo de titulación presentado como requisito para la obtención del título de Químico

Autor:

Jhonny Mauricio Aldás Bedón

Tutor:

Hortensia María Rodríguez Cabrera, PhD

Co-tutor:

Reinier Lemos García, MSc

Urcuquí, julio 2022

SECRETARÍA GENERAL
ESCUELA DE CIENCIAS QUÍMICAS E INGENIERÍA
CARRERA DE QUÍMICA
ACTA DE DEFENSA No. UITEY-CHE-2022-00036-AD

En la ciudad de San Miguel de Urcuquí, Provincia de Imbabura, a los 25 días del mes de julio de 2022, a las 14:00 horas, en el Aula 1 de la Universidad de Investigación de Tecnología Experimental Yachay y ante el Tribunal Calificador, integrado por los docentes:

Presidente Tribunal de Defensa	Dr. TERENCIO THIBAULT , Ph.D.
Miembro No Tutor	Dr. CAETANO SOUSA MANUEL , Ph.D.
Tutor	Dra. RODRIGUEZ CABRERA, HORTENSIA MARIA , Ph.D.

Se presenta el(la) señor(ita) estudiante **ALDAS BEDON, JHONNY MAURICIO**, con cédula de identidad No. **1004414478**, de la **ESCUELA DE CIENCIAS QUÍMICAS E INGENIERÍA**, de la Carrera de **QUÍMICA**, aprobada por el Consejo de Educación Superior (CES), mediante Resolución **RPC-SO-39-No.456-2014**, con el objeto de rendir la sustentación de su trabajo de titulación denominado: **The Unusual Behavior of Galactose-steroid Bingel-Hirsch Reaction for Functionalization of C60-fullerene: A Theoretical Study.** , previa a la obtención del título de **QUÍMICO/A**.

El citado trabajo de titulación, fue debidamente aprobado por el(los) docente(s):

Tutor	Dra. RODRIGUEZ CABRERA, HORTENSIA MARIA , Ph.D.

Y recibió las observaciones de los otros miembros del Tribunal Calificador, las mismas que han sido incorporadas por el(la) estudiante.

Previamente cumplidos los requisitos legales y reglamentarios, el trabajo de titulación fue sustentado por el(la) estudiante y examinado por los miembros del Tribunal Calificador. Escuchada la sustentación del trabajo de titulación, que integró la exposición de el(la) estudiante sobre el contenido de la misma y las preguntas formuladas por los miembros del Tribunal, se califica la sustentación del trabajo de titulación con las siguientes calificaciones:

Tipo	Docente	Calificación
Presidente Tribunal De Defensa	Dr. TERENCIO THIBAULT , Ph.D.	10,0
Tutor	Dra. RODRIGUEZ CABRERA, HORTENSIA MARIA , Ph.D.	10,0
Miembro Tribunal De Defensa	Dr. CAETANO SOUSA MANUEL , Ph.D.	10,0

Lo que da un promedio de: **10 (Diez punto Cero)**, sobre 10 (diez), equivalente a: **APROBADO**

Para constancia de lo actuado, firman los miembros del Tribunal Calificador, el/la estudiante y el/la secretario ad-hoc.

ALDAS BEDON, JHONNY MAURICIO
Estudiante

Dr. TERENCIO THIBAULT , Ph.D.
Presidente Tribunal de Defensa

Dra. RODRIGUEZ CABRERA, HORTENSIA MARIA , Ph.D.
Tutor

Dr. CAETANO SOUSA MANUEL , Ph.D.
Miembro No Tutor

YEPEZ MERLO, MARIELA SOLEDAD
Secretario Ad-hoc

AUTORÍA

Yo, **Jhonny Mauricio Aldás Bedón**, con cédula de identidad **100441447-8**, declaro que las ideas, juicios, valoraciones, interpretaciones, consultas bibliográficas, definiciones y conceptualizaciones expuestas en el presente trabajo; así cómo, los procedimientos y herramientas utilizadas en la investigación, son de absoluta responsabilidad de el/la autora del trabajo de integración curricular. Así mismo, me acojo a los reglamentos internos de la Universidad de Investigación de Tecnología Experimental Yachay.

Urcuquí, julio 2022.

Firmado electrónicamente por:
JHONNY
MAURICIO
ALDAS BEDON

———————————————————

Jhonny Mauricio Aldás Bedón

CI: 100441447-8

AUTORIZACIÓN DE PUBLICACIÓN

Yo, **Jhonny Mauricio Aldás Bedón,** con cédula de identidad 100441447-8, cedo a la Universidad de Investigación de Tecnología Experimental Yachay, los derechos de publicación de la presente obra, sin que deba haber un reconocimiento económico por este concepto. Declaro además que el texto del presente trabajo de titulación no podrá ser cedido a ninguna empresa editorial para su publicación u otros fines, sin contar previamente con la autorización escrita de la Universidad.

Asimismo, autorizo a la Universidad que realice la digitalización y publicación de este trabajo de integración curricular en el repositorio virtual, de conformidad a lo dispuesto en el Art. 144 de la Ley Orgánica de Educación Superior.

Urcuquí, julio 2022.

Firmado electrónicamente por:
**JHONNY
MAURICIO
ALDAS BEDON**

_____

Jhonny Mauricio Aldás Bedón

CI: 100441447-8

DEDICATION

To my incomparable God.

To my parents, Carmela and Segundo.

To my brothers and sisters.

To my whole family.

To my professors.

Jhonny Mauricio Aldás Bedón

ACKNOWLEDGMENT

RESUMEN

El [60] fullereno es una molécula que ha sido funcionalizada para modificar sus propiedades químicas como la solubilidad y explorar sus aplicaciones biológicas y en ciencia de los materiales. Esta molécula ha sido funcionalizada exoédricamente con grupos hidrofílicos como aminoácidos, péptidos, esteroides y azúcares, para mejorar su hidrofobicidad y biocompatibilidad. La reacción de Bingel-Hirsch es eficiente para la ciclopropanación regioselectiva del C_{60} a metanofullereno, a partir de derivados de ésteres malónicos, 1,8-Diazabiciclo[5.4.0]undec-7-eno (DBU) como base y tetrabromuro de carbono (CBr_4). Es una estrategia alternativa a la reacción propuesta por Bingel, que promueve la generación del intermedio monohalomalonato reactivo *in situ*. En esta investigación, se estudia la reacción de Bingel-Hirsch del derivado del éster malónico de D-galactosa-diosgenina y el C_{60}. Los resultados mostraron que el producto esperado sufre la hidrólisis del éster promoviendo la liberación de galactosa, seguida de la descarboxilación para obtener un híbrido diosgenina-C_{60}. Se presenta además una caracterización exhaustiva del producto final mediante espectroscopía IR, NMR y espectrometría de masas. Con base en los resultados experimentales, se propone un mecanismo en el que la DBU protonada ($DBUH^+$) o trazas de H_3O^+, ambos posibles subproductos en el procedimiento de Bingel-Hirsch, donan un protón para asistir la hidrólisis catalizada por ácido a través de un mecanismo unimolecular de escisión de alquilo $A_{AL}1$, debido a la liberación de un carbocatión en el fragmento de galactosa altamente estable. Los cálculos teóricos en el nivel de teoría DFT PBE/6-31G predicen las geometrías estructurales más estables para los compuestos involucrados en los mecanismos propuestos. Se investigaron parámetros estereoelectrónicos relevantes considerando descriptores y propiedades seleccionadas como la polarizabilidad, el momento dipolar, la lipofilia y el área de superficie polar topológica, mostrando que la hidrólisis y la descarboxilación posterior no causan cambios drásticos en las propiedades analizadas. Además, el método semiempírico PM3 se utiliza para calcular el perfil de energía potencial (PEP) de la hidrólisis catalizada por ácido del híbrido galactosa-diosgenina-[60] fullereno por $DBUH^+$ o H_3O^+ en fase gaseosa. De acuerdo con los PEP obtenidos, se observa que la hidrólisis responde a un proceso bimodal y se favorece termodinámica y cinéticamente con H_3O^+.

Palabras clave: Reacción de Bingel-Hirsch; mecanismos de hidrólisis; catálisis ácida; cálculos teóricos.

ABSTRACT

The [60] fullerene is a molecule that has been functionalized to modify its chemical properties such as solubility and explore its biological and materials science applications. It has been exohedrally functionalized with hydrophilic groups, i.e., amino acids, peptides, steroids and sugars, which improves its hydrophilicity and biocompatibility. The Bingel-Hirsch reaction is an efficient tool for the regioselective cyclopropanation of C_{60} to methanofullerene, starting from malonic esters derivatives, 1,8-Diazabicyclo[5.4.0]undec-7-ene (DBU) as base and carbon tetrabromide (CBr_4). It is an alternative strategy to the Bingel reaction, proposing the generation of the reactive monohalomalonate intermediate *in situ*. Herein, a Bingel-Hirsch reaction of D-galactose-diosgenin malonic ester derivatives is studied. The results showed that the awaited product suffers the ester hydrolysis promoting the Galactose release, followed by decarboxylation to obtain a Diosgenin-C60 hybrid. The full characterization of the final product through IR, NMR, and MALDI-TOF spectrometry is presented. Based on the experimental results, a plausible mechanism is proposed in which a $DBUH^+$ or traces of H_3O^+, both possible byproducts in the Bingel-Hirsch procedure, to donate a proton to improve the observed acid-catalyzed hydrolysis through a unimolecular alkyl cleavage $A_{AL}1$ mechanism because the highly stable galactose cation release. Theoretical calculations at the DFT PBE/6-31G level of theory predict the most stable structural geometries for all compounds involved in the proposed mechanisms. Relevant stereoelectronic parameters were investigated considering selected descriptors and properties, namely polarizability, dipole moment, lipophilicity, and topological polar surface area, showing that the hydrolysis and subsequent decarboxylation do not cause drastic changes in the properties analyzed. In addition, the PM3 semi-empirical method is used to calculate the Potential Energy Profile (PEP) of the acid-catalyzed hydrolysis of the galactose-diosgenin-fullerene hybrid by $DBUH^+$ or H_3O^+ in the gas phase. According to the PEP, it is observed that hydrolysis responds to a bimodal process, and is thermodynamically favored with H_3O^+.

Keywords: Bingel-Hirsch reaction; hydrolysis mechanisms; acidic catalysis; theoretical calculations.

Table of Contents

List of Figures

List of Tables

Abbreviations

DSG	Diosgenin
DBU	1,8-Diazabicyclo[5.4.0]undec-7-ene
DBUH$^+$	Protonated DBU
A$_{AC}$	Acyl-Oxygen Bond Cleavage
QM	Quantum Mechanics
DFT	Density Functional Theory
PBE	Perdew–Burke–Ernzerhof
D3BJ	D3 with Becke-Johnson damping
PM3	Parametric Method 3
GGA	Generalized Gradient Approximation
IUPAC	International Union of Pure and Applied Chemistry
PES	Potential Energy Surface
TS	Transition State
INT	Intermediate
IRC	Intrinsic Reaction Coordinate
HRMS	High Resolution Mass Spectroscopy
2C	61-(D-Galactopyranose, 2,3,4,6-tetraacetate)-61-(3β-O-carbetoxy-25R-spirost-5-en)methano[60]fullerene
SASA	Solvent-Accessible Surface Area
TPSA	Topological Surface Area
Hy	Hydrophilic index
logP$_{ow}$	Octanol/Water Partition Coefficient
LUMO	Lowest Unoccupied Molecular Orbitals
HOMO	Highest Occupied Molecular Orbitals
EPM	Electrostatic Potential Map
PED	Potential Energy Diagram

1. Chapter I. Introduction

1.1. Monosaccharides: D-galactose

Monosaccharides are the simplest carbohydrate molecules. The term monosaccharide indicates it is a molecule composed of only one sugar unit. These structures are the building blocks of bigger structures like oligosaccharides and polysaccharides. The backbone carbon atom is completely functionalized with hydroxyl groups and a carbonyl oxygen atom. Moreover, there are a significant number of chiral carbons. Each chiral carbon atom contributes to a total number of 2^n of possible conformations[1].

Monosaccharides are classified according to three different characteristics: the position of the carbonyl group, the number of carbon atoms, and its chiral handedness. Considering the position of the carbonyl group, they are divided as aldoses(when the aldehyde group is present) or ketoses (when a ketone group is present). The monosaccharides are also classified as pentoses or hexoses depending on their length chain of five or six carbon atoms. Regarding chirality, those monosaccharides are named D- or L-sugars when the hydroxyl group on the highest-numbered chiral atom is located on the right- or the left-hand side respectively[1]. For a monosaccharide solution, the linear structure (Fischer projection) is in equilibrium with cyclic forms α and β configurations[2] (Haworth projection).

The most widely distributed carbohydrate is D-glucose, an aldose of six-carbon chain atoms (hexose). Due to the interest of our research, we focus on D-galactose, a glucose epimer, because they only differ in the carbon four configuration. Figure 1 shows the structures and the open and close chain equilibrium for D-glucose and D-galactose.
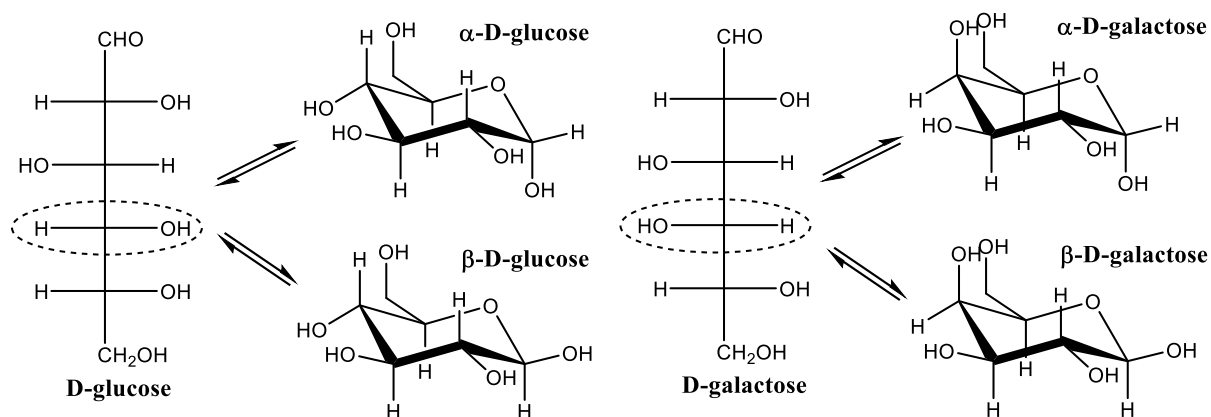
Figure 1 Open and closed chain equilibria of D-glucose and D-galactose

1

Galactose and other carbohydrates are involved in critical biological functions such as energy production, storage, and transport; regulation of cholesterol and triglyceride; glycan synthesis and glycosylation; regulation of glycemia and fermentation processes[3]. D-galactose's molecular structure and its solubility allow diffusion across the membranes, making it a suitable candidate for biological applications[3]. The chronic administration of D-galactose has been used to induce premature cardiac and brain aging processes in animal models[4].

1.2. Steroids: diosgenin (DSG)

Steroids are molecules consisting of four rings in a perhydrocyclopentano[α]phenanthrene orientation. Saponins are a glycosides group composed of a steroidal or triterpenoid skeleton and a sugar residue. In the case of steroidal saponins, they have 27 carbon atoms in their frame and are classified into spirostan, furostan, and cholestan saponins[5]. Spirostan saponin contains an aglycone formed by four-six membered and two five-membered rings (labeled as A, B, C, D, E, and F-rings), as shown in Figure 2.

Diosgenin (DSG), named by the IUPAC as (25R)-spirost-5-en-3β-ol, is a spirostan-type saponin, and it is one of the most known steroid saponins in medicinal plants. DSG is highly hydrophobic and presents poor water solubility[7]. It shows interesting properties such as anti-inflammatory and antioxidant. Besides, it can be employed in blood and cerebral disorders, allergic diseases, diabetes and obesity, menopausal symptoms, and skin aging; it can also be a protector agent for cardiovascular diseases and, prominently, cancer[6]. The biological application of DSG can be influenced by the carbohydrate moieties present on it[7]. The molecular structure of diosgenin is shown in Figure 2.
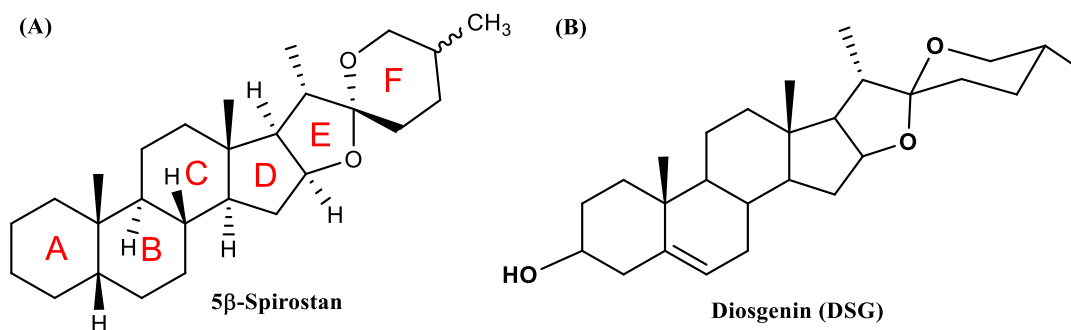
Figure 2 Molecular Structure of (A) steroidal saponin, and (B) diosgenin (DSG)

2

1.3. Fullerene and derivatives

In 1970 Osawa theoretically predicted the existence of polyhedral carbon cluster and some of their properties[8]. Fifteen years later, Kroto *et al.*[9] showed the existence of [60] fullerene, and since it, several organic derivatives have been synthesized with promising applications in medicinal chemistry and materials science[10–12]. The C_{60} is formed by 60 carbon atoms with C_5-C_5 single bonds, which comprise 12 pentagons, and C_5-C_6 double bonds, forming 20 hexagons[13]. There are two types of bonds determined using the X-Ray crystal structure of fullerene and some derivatives: the first one, named short bonds or 6,6 junctions, is shared by two hexagons and measures 1.38 Å long, and the second one is called long or 5,6 junctions shared by a hexagon and a pentagon which measures 1.45 Å long[14]. All the rings are fused, and all the double bonds are conjugated. Even though they have a high conjugation with sp^2 carbons, they behave chemically and physically as electron-deficient systems[15], as was demonstrated by their high electron affinity in the gas phase and good oxidizing power in solution[15,16]. The spherical shape of fullerene demands large strain energy, and the curvature induces pyramidalization of carbon atoms, weakening π-conjugation[17]. [60] Fullerene is composed of three different structural components, as shown in Figure 3.
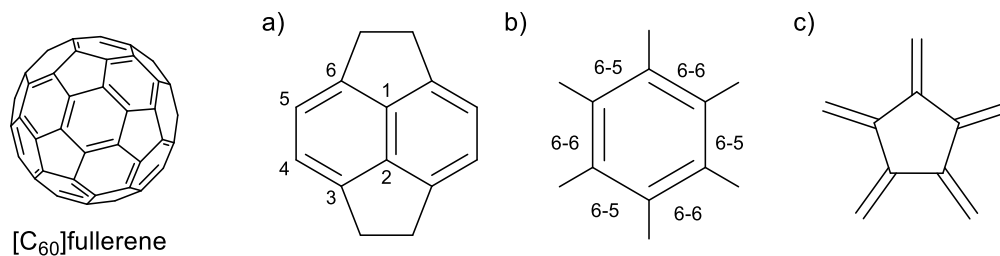
Figure 3 Molecular structures of [C$_{60}$] fullerene and its structural components: a) pyracelenic unit, b) cyclohexatriene, and c) [5]-radialene.

The molecules derived from graphene are [C_{60}] fullerene and carbon nanotubes (CNTs). These nanostructures have been widely investigated to explore their potential applications. Their chemical reactivity of the external surface is predicted by the pyramidalization angle (Θ_P) of a carbon atom, defined as the difference between the orbital π and σ bond minus 90° ($\Theta = \Theta_{\pi\sigma} - 90°$)[17–19]. A more significant value for the pyramidalization angle indicates a higher reactivity for addition reactions of fullerenes and CNTs[17]. In addition, the π-orbital misalignment angle (φ) also influences reactivity for CNTs[19]. The carbon atom hybridization for CNTs and graphene is

3

also sp^2 but it is deformed for the curvature of their shapes which also influences their reactivity. A greater tension due to its curvatures implies a higher reactivity[19]. According to the reported values of Θ_P, the reactivity order of these molecules is given as fullerene>nanotubes>graphene[17–19].

The C_{60} presents some interesting characteristics, such as the generation of oxygen species as potential candidates for photodynamic therapy when exposed to visible light. The acute toxicity of water-soluble fullerenes is reported to be low[20]. Fullerene is not soluble in polar solvents, limiting its use in pharmaceutical and biological applications. One strategy to overcome this problem is functionalizing C_{60} with hydrophilic groups[10] such as amino acids, peptides, steroids, and sugars[21]. For instance, the conjugation of saccharides with C_{60} improves hydrophilicity and biocompatibility[21]. In addition, it is thought that fullerene-sugar hybrids may show biological activities since carbohydrate moieties are involved in specific molecular recognition process[22].

1.4. Fullerene Hybrids and their applications

The synthesis of [60] fullerene-steroid hybrids has been reported, and theoretical studies have suggested a potential use as human immunodeficiency virus-1 (HIV-1) protease inhibitors[12,23]. Other research indicates that fullerene-sugar derivatives inhibit the enzyme activities of HIV-1 protease efficiently in living cells under the influence of visible light irradiation[24]. Liu and coworkers[25] functionalized C_{60} with polyethylene glycol (PEG) to improve its solubility and accumulate in the tumor tissue and diethylenetriaminepentaacetic acid (DTPA) to chelate with Gd^{3+}, obtaining the complex C_{60}-PEG-DPTA-Gd, which demonstrated to be an excellent candidate as a photosensitizer for photodynamic therapy of cancer[25]. Theoretical studies indicate that the functionalization of dihydroartemisinin on fullerene would increase its efficiency against malaria and its ability to accept and donate electrons[26]. Highly soluble sugar-fullerene hybrids produce cancer cell death when exposed to visible light[21]. A suitable formulation for use in pharmaceuticals is lipofullerene-saccharide conjugate as antimetastatic agents that help in the reduction and/or elimination of the spread of neoplasms in mammalian systems[27].

Besides, fullerene oxide silica composite as a stationary phase for high-performance liquid chromatography (HPLC) shows excellent selectivity and retention for a wide range of polar molecules[28]. More medical applications such as DNA photocleavage, free radical scavenger, antimicrobial activity, osteoporosis[20], antioxidant and neuroprotective activity[29] have been

4

reported associated to fullerene derivatives. Furthermore, fullerene derivatives have applications related to polymers, thin films, electro-optical devices, liquid crystals, fluorescence, catalysis, purification, and radioprotection, among others[14,30].

1.5. Reactions to fullerene functionalization: Prato and Bingel-Hirsch reaction

Some of the common reactions to obtain mono adducts of fullerenes are the well-known Prato and Bingel protocols. The reactions were described by Maurizio Prato[14] and Carsten Bingel[11], respectively. Both procedures promote the introduction of functional groups on the fullerene in a simple, one-step process, allowing the extensive use of these reactions to obtain a wide variety of fullerene derivatives[31].

The Prato reaction is a 1,3-dipolar cycloaddition of an azomethine ylide to the double bond in a 6,6 ring position in fullerene, giving a stable pyrrolidinofullerene[32,33]. The ylide is generated by condensation of a sarcosine derivative with an aldehyde heated at reflux in toluene. Figure 4 shows the general scheme for Prato reaction[34].
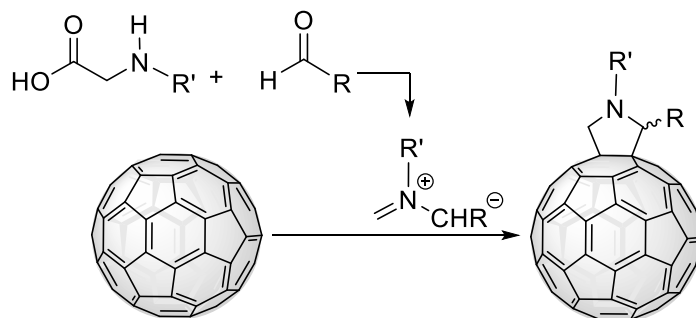
Figure 4 General Prato reaction

On the other hand, the Bingel reaction is the cyclopropanation of fullerene to methanofullerene through the reaction of C_{60} with the bromo derivative of diethyl malonate, under basic conditions as sodium hydride (NaH) or 1,8-diazabicyclo[5.4.0]undec-7-ene (DBU), at room temperature, first discovered by C. Bingel in 1993[32]. Alternative strategies to generate reactive monohalomalonate intermediate *in situ* have been introduced by Hirsch[32,33] and are extensively known as Bingel-Hirsh reaction[12]. This reaction is a selective addition to [6,6] position on the fullerene scaffold. It requires only mild conditions giving excellent yields, and the ester can be conveniently modified [32,33]. The Bingel-Hirsch reaction occurs under more favorable conditions

compared to that of the Prato reaction, which proceeds at a higher temperature (~ 110°C)[12,13,32,35]. The Bingel-Hirsch reaction is shown in Figure 5.
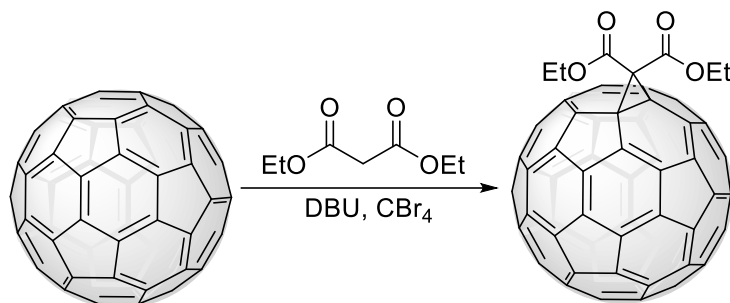
Figure 5 General Bingel-Hirsch reaction

1.6. Ester Hydrolysis

Ester hydrolysis is the most studied nucleophilic acyl substitution[36]. It is known that esters can be irreversibly hydrolyzed via basic conditions or reversibly under acid media[36].

1.6.1. Acid catalyzed ester hydrolysis mechanisms

Ingold has classified the acid-catalyzed ester hydrolysis into four mechanisms $A_{AC}1$, $A_{AC}2$, $A_{AL}1$, and $A_{AL}2$ are shown in Figure 6 [36–38]. A shorthand notation is used where A refers to acidic medium; the subscripts AC and AL refer to acyl- and alkyl-oxygen bond cleavage, respectively. The numbers 1 and 2 indicate the reaction molecularity.

The $A_{AC}2$ mechanism is the most common acid-catalyzed hydrolysis route. It occurs through an H_2O addition reaction in the acid-activated ester, forming the tetrahedral intermediate and R'-OH cleavage. Low pKa values block the $A_{AC}2$ pathway, but general acid catalysis is possible. The other acid-promoted paths are possible under specific features reaction. For example, the $A_{AC}1$ and $A_{AL}1$ mechanisms are classified as S_N1 reactions. The $A_{AC}1$ mechanism, the second acid-assisted ester hydrolysis involving the acyl cleavage, could be observed for sterically hindered R and in ionizing solvents. The $A_{AL}1$ mechanism, which consists of the alkyl oxygen cleavage where an acyloxy group OCOR or its conjugated acid is the leaving group[36] is favored if R' gives a stable carbocation [37]. Finally, the $A_{AL}2$ mechanism is not commonly observed due to the requirements of H_2O as the nucleophile in an S_N2 reaction. [39,40]. All described mechanisms are shown in Table 1.
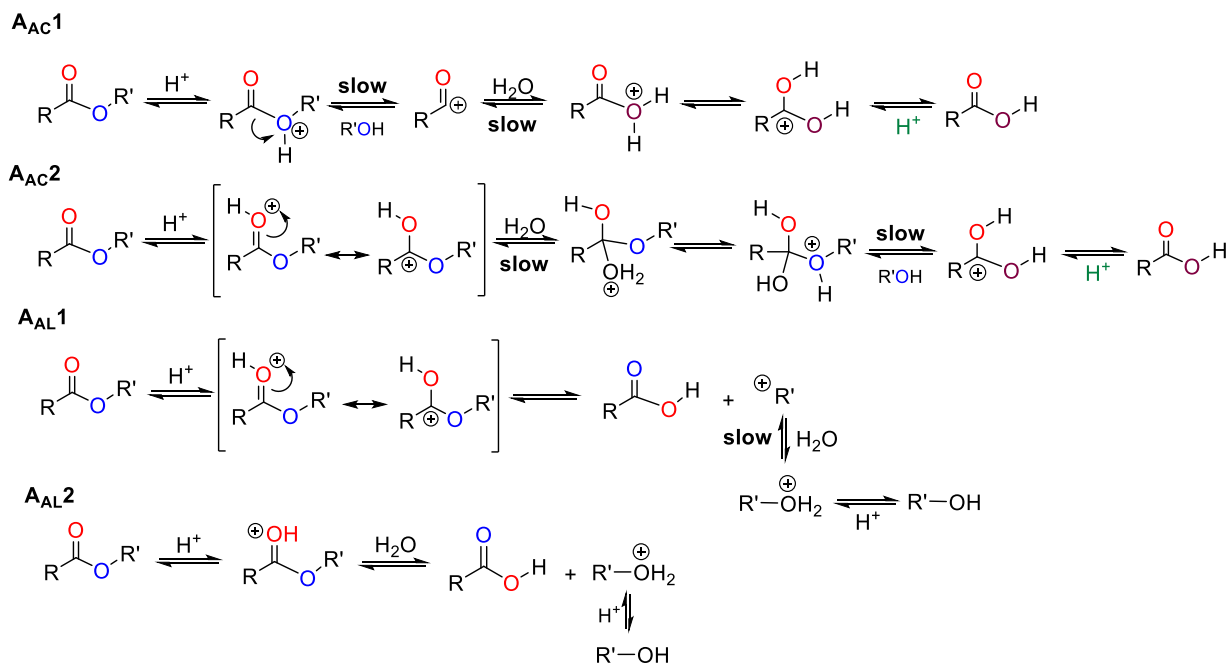
Figure 6 Acid-catalyzed ester hydrolysis mechanisms.

Table 1 Description of the four mechanisms for the acid-catalyzed ester hydrolysis [36–38]

Name		Reaction Conditions
Ingold	Type	
$A_{AC}1$	S_N1	* To very bulky R * In ionizing solvents * Presence of a strong acid * Rare
$A_{AC}2$	Tetrahedral	* Blocked by low pK_a values * Most common
$A_{AL}1$	S_N1	* R' comes off as a stable carbocation such as esters of tertiary alcohols * Common
$A_{AL}2$	S_N2	* H$_2$O must act as a nucleophile * For the acid cleavage of γ-lactones * Rare

1.7. Computational Approach

Computational chemistry has become a crucial area for chemists. Experimental chemists often use computational chemistry to overcome problems encountered in the laboratory and support explanations. This area involves calculations of quantum mechanics (QM or ab initio methods) and molecular mechanics (MM). QM calculations comprise methods of theoretical chemistry

7

such as Hartree-Fock (HF), post-Hartree-Fock, and DFT methods that describe the molecular geometry, electronic properties, and reaction pathways for large systems comprising up to a hundred atoms[41]. DFT has become very popular in performing computational chemistry approaches.

On the other hand, MM calculations help to study bigger systems, such as the binding interaction of a ligand molecule with a drug target[42]. The molecular dynamics (MD) use MM methods to study the motion of atoms in a determined system over time[41,43]. In this way, computational chemistry is a powerful tool for obtaining reasonable approximations, reducing experimental risks, and a considerable accuracy and better comprehension of reactions at the atomic level. Nevertheless, some disadvantages are limitations in describing intermolecular interactions, experience in selecting appropriate methods, accuracy based on functional, basis set and solvation model, and high computational cost[41].

Moreover, there are the quantum-chemical semiempirical methods which begin from ab initio principles and then introduce integral approximations and parametrizations to accelerate calculations[44]. They lose accuracy but win efficiency to calculate large systems. One of the most used semiempirical methods has been the Parametric Method 3 (PM3)[44], which allows the calculation of many molecular properties. The PM3 method uses a minimal basis set of valence Slater type s and p atomic orbitals[45]. Although PM3 is not an accurate method to obtain reaction energies, it is a good first approach to describe bond braking and bond forming reactions[45,46].

1.7.1. DFT methods

Density functional theory (DFT) is a quantum-mechanical (QM) method used to obtain information of molecules and materials about the electronic structure, geometric parameters and determine the reaction mechanisms. There are several approximations to get the exchange-correlation energy and calculate molecular properties at various levels of accuracy using different functionals or methods. According to John Perdew, the "Jacob's Ladder" starts from the Hartree world to the "Heaven" of chemical accuracy[47]. The ladder has five rungs; on the lower rung, the less accurate method named local spin-density (LSD) approximation of Kohn and Sham, on the second rung the generalized gradient proximation (GGA), on the third rung the meta-GGA, and rung four the hybrid or hyper-GGA methods[47,48]. There is no agreement on the fifth rung; however, it is labeled as doubly hybrid approximation (DHA), which includes the

information of the unoccupied Kohn-Sham orbitals[48]. DFT tries to overcome the inaccuracy of Hartree-Fock and the high computational cost of post-Hartree-Fock methods.

1.7.2. DFT basis sets

A basis set is a group of linearly combined functions used for approximate theoretical calculations or modeling molecular orbitals (MOs)[45]. These functions represent the unknown MOs utilizing a set of known functions. Several functions could be used, such as exponential, Gaussian, polynomial, cube functions, wavelets, or plane waves[49]. Basis sets can generally be classified as minimal basis sets, Pople basis sets, Correlation consistent basis sets, double, triple, quadruple zeta basis sets, and Plane-wave basis sets.

Minimal basis sets involve selecting one basis function for every atomic orbital necessary to describe the free atom[45]. Pople and coworkers developed the most used minimal basis set, the Slater Type Orbital-nGaussian (STO-nG) basis sets where a linear combination of "n" Gaussian Type Orbitals fitted to each STO[45].

Moreover, k-$nmlG$ bais sets were also developed by Pople and coworkers. These Pople basis sets are classified as split valence type. The letter k indicates the number of Primitive Gaussian Type Orbitals (PGTOs) for representing the core orbitals; the letters nml indicate both the number of functions the valence orbitals are split into and PGTOs for their representation[46]. Two numbers (nl) indicate a split valence but three numbers (nml) indicate a triple split valence[46]. Furthermore, G stands for Gaussian and before that we can include diffuse function and after the polarization functions. Diffuse functions which are generally s- and p- functions[46] are used to obtain more accurate results of molecular properties such as dipole and quadrupole moments[50]. Polarization functions represent the charge polarization at the Hartree-Fock level and the electron correlation at correlated levels[50]. They contribute to a better description of molecular geometry and energies[45].

The correlation consistent (cc) basis sets were designed by Dunning and coworkers. All the functions of the cc basis sets that contribute similar quantities of correlation energy work at the same stage[46]. Moreover, they include directly polarization functions. There are various cc basis sets depending of the final number of contracted functions (n). The basis sets are cc-pVnZ (correlation consistent polarized Valence n-Zeta), with n = Double (D), Triple, (T), Quadruple (Q), Quintuple (5) or Sextuple (6)[51].

Plane wave basis sets were designed for the simulation of molecules and condensed phase systems[52]. They are based on the linear combination of plane waves (PW) which have been widely used in solid state simulations[52]. Within the approach of PW, it is used pseudopotentials to treat core electrons since they are not included explicitly. Some advantages of PW are calculations can be executed in the reciprocal or direct space, easy control of the convergence and independence on the position of atoms[53].

For large organic or biological molecules, small basis such as Pople basis sets are adequate[54], although it would be better to use bigger ones. The 6-311G basis set, a small-sized Pople-type basis set, has been employed for hybrid fullerene systems[12,23,55,56]. Some articles report theoretical calculations of fullerene hybrids using the PBE/6-31G(d) method[12,57]. The basis set 6-31G(d,p) is suitable for calculations[23] of fullerene systems because it gives accuracy and computational efficiency[56].

1.7.3. Geometry Optimization

The structure of a molecule can be described by the spatial distribution of the atoms in the molecule. Every structure has a specific set of coordinates related to the atoms. In this way, the proportioned structure and its electronic pattern had a particular energy[58]. Potential energy surface (PES) is defined as the energy as a function of the structure for a particular state of the molecule and depends on the coordinates of the atoms in the space. Figure 7 represents a model PES depicted as a hilly landscape with valleys, peaks, and mountain passes. The model PES is a 3D representation to illustrate minimum configurations, transition structures, reaction paths and so on[58]. The plot contains two geometric variables on the x and y-axis in function of the energy, the z-axis. The transition state (TS) is also termed a first-order saddle point. It is a maximum in one direction (along the reaction path) and a minimum in all other orientations (orientations perpendicular to the reaction path); a second-order saddle point is a maximum in two directions and a minimum in all the remaining orientations[58]. A minimum is distinguished because the gradient is zero and the Hessian has only positive eigenvalues which correspond to molecular vibrations[58]. The valleys of a PES indicate reactants, intermediates, and products of a reaction. Indeed, the minimum of the valley represents the equilibrium structure. Then, geometry optimization serves to find these minimums for the intended reaction.
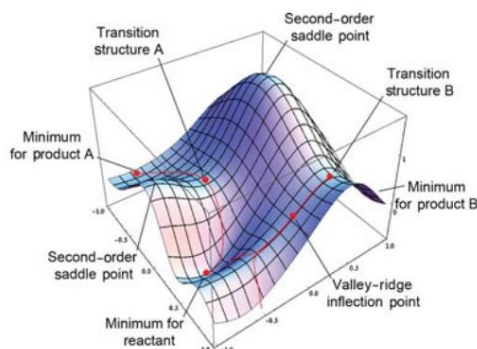
Figure 7 Potential energy surface (PES) indicating minimum, transition structures, second-order saddle points, and reaction paths (from ref. 58 with permission from John Wiley and Sons).

1.7.4. Frequency Calculations

Vibrational frequencies describe the vibrations of atoms at their equilibrium position. The DFT theory uses a zero-temperature approach however we can also establish a temperature to execute calculations. It means that computational calculations predict the properties of molecules at equilibrium or minimum energy positions[59]. Vibrational frequencies are evaluated at the equilibrium geometry. Once the structure is correctly optimized, the frequency calculations are performed. The obtained vibrations represent the theoretical spectrum, indicating if the optimized structures correspond to a minimum. A structure corresponds to a minimum if there is no negative frequency only, to a saddle point if there is one negative frequency, and to a higher-order critical point if there is more than one negative frequency.

1.7.5. Mechanism Calculations

The reaction mechanism describes the reaction path from reactants through transition states or first-order saddle points and intermediates (if any) to products. The steepest descent reaction path from the TS down to the reactants and the products is the minimum energy path (MEP) or the intrinsic reaction coordinate (IRC)[58]. A TS is characterized by a zero gradient and a Hessian that has only one negative eigenvalue which means that a TS has only one vibrational frequency[58]. There are three main methods to find saddle point optimizations: a relaxed surface scan, a transition state optimization (OptTS) and the nudged elastic band method (NEB).

First, run a relaxed surface scan for a proposed geometry close to the transition state. A relaxed surface scan involves constrained optimizations for different values of a reaction coordinate[60]. It

11

means to scan through one variable while all others are relaxed[60]. Second, the transition state optimization (OptTS) method is more convenient when the geometry is very close to the saddle point state, and it can use an approximate or exact Hessian. The OptTS method uses the eigenvector following algorithm to calculate the nearest stationary point on PES[61]. Finally, the nudged elastic band method (NEB) minimizes the elastic band until it converges to the minimum energy path.

1.8. Problem statement

[60] Fullerene is one of the crucial discoveries in chemistry due to its multiple promising applications. Due to its hydrophobicity, there are limitations for biological applications. One alternative to overcome its insolubility is the fullerene functionalization with hydrophilic compounds such as amino acids, carboxylic acids, sugars, steroids, polyhydroxy groups, or amphiphilic polymers. In this way, a fullerene functionalization using steroid-sugar malonate is pursued by employing the Bingel-Hirsch protocol. The research group of Suarez *et al.*[62] successfully formed monosaccharide-diosgenin fullerene hybrids; however, when D-galactose was used as a sugar scaffold, the isolated product did not correspond to the expected D-galactose-diosgenin fullerene hybrid, and a diosgenin-fullerene derivative was obtained as shown in Figure 8.
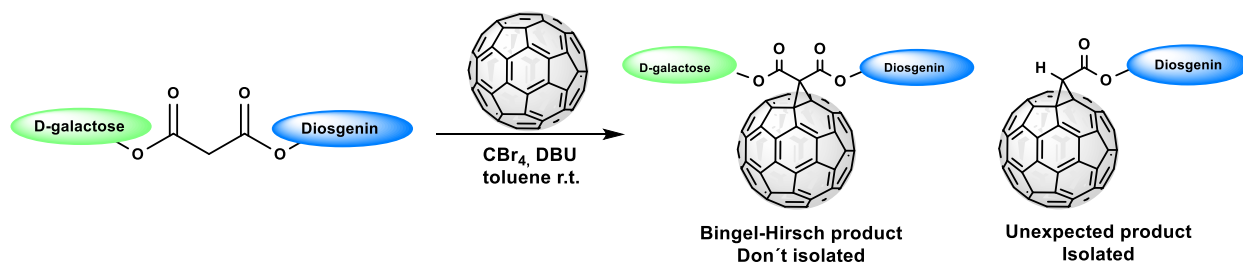
Figure 8 Bingel-Hirsch reaction of D-galactose-diosgenin malonate hybrid and C$_{60}$.

This study aims to have a theoretical approach that allows us to explain the unusual behavior observed in galactose-diosgenin-fullerene hybrid synthesis under Bingel-Hirsch conditions.

1.9. Objectives

1.9.1. General Objective

- To study the Bingel reaction between the fullerene and D-galactose-diosgenin malonate focusing on the unusual behavior of the D-galactose-diosgenin-fullerene hybrid.

1.9.2. Specific Objectives

- To describe the unusual behavior observed in the Bingel reaction of the D-galactose-diosgenin malonate and fullerene.

- To propose a mechanism that allows explaining the experimental results.

- To use theoretical calculations that support the observed results using DFT for geometry optimization, FT-IR simulation, and mechanism calculation.

2. Chapter II Materials and Method

2.1. Methodology

This work describes the Bingel-Hirsch reaction of D-galactose-diosgenin malonate and fullerene. In addition, theoretical calculations are used to support the experimental results. The overall workflow of this work is shown in Figure 9.
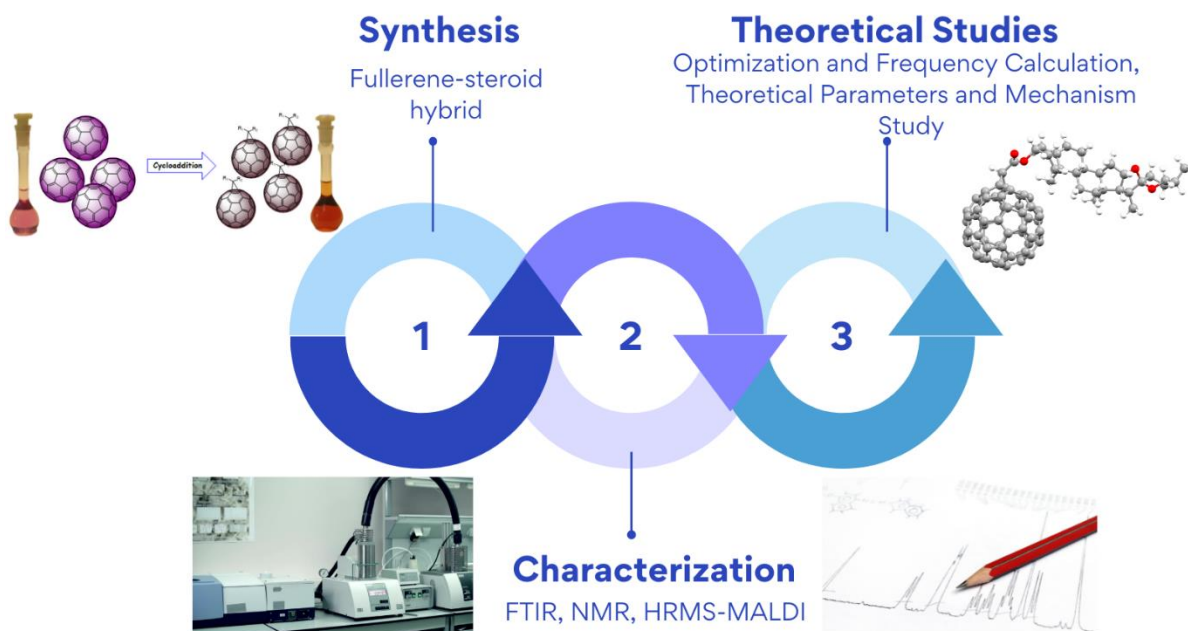
Figure 9 General methodology of the Research Project.

The reagents used in the Bingel-Hirsch reaction of D-galactose-diosgenin and fullerene are summarized in Table 2.

Table 2 Reagents used for the Bingel reaction of the D-galactose-diosgenin malonate and fullerene

Reagents
[60] Fullerene
Carbon tetrabromide (**CBr$_4$**)
1,8-Diazabicyclo[5.4.0]undec-7-ene (**DBU**)
Toluene
D-Galactopyranose, 2,3,4,6-tetraacetate-diosgenin-malonate (**1**)

2.2. Synthesis and characterization of the 61-(3β-O-carbetoxy-25R-spirost-5-en)methano[60]fullerene (4)

The synthesis of 61-(3β-O-carbetoxy-25R-spirost-5-en)methano[60]fullerene (4) was done following the Bingel-Hirsch protocol. First, 0.06 g (0.08 mmol) of fullerene was dissolved in 50 mL of toluene. Then, it is added 0.069 g (0.08 mmol) of D-Galactopyranose, 2,3,4,6-tetraacetate-diosgenin-malonate (abbreviated 1). In another step, 0.05 g of (0.12 mmol) of CBr$_4$ and 0.12 mL (1.35 mmol) of 1,8-Diazabicyclo[5.4.0]undec-7-ene (DBU) were added. The reaction mixture is cooled down in an ice bath and stirred for 90 minutes under an Argon atmosphere. After 1.5 hours, water is added, and the organic and aqueous phases are separated. The organic extract is dried with anhydrous MgSO$_4$, and the organic solvent is rotoevaporated. Finally, isolation and purification of the product is done with column chromatography employing CS$_2$ to elute unreacted C$_{60}$ and DCM for the corresponding hybrid. The final product **4** was characterized using Fourier Transform Infrared (FTIR), ^{1}H and ^{13}C Nuclear Magnetic Resonance (NMR), and High Resolution Mass Spectroscopy (HRMS) under MALDI-TOF (dithranol as matrix) conditions which allowed to elucidate the structure, which is shown in Figure 10. The synthesis and characterization were done by the research group of Suarez *et al*.
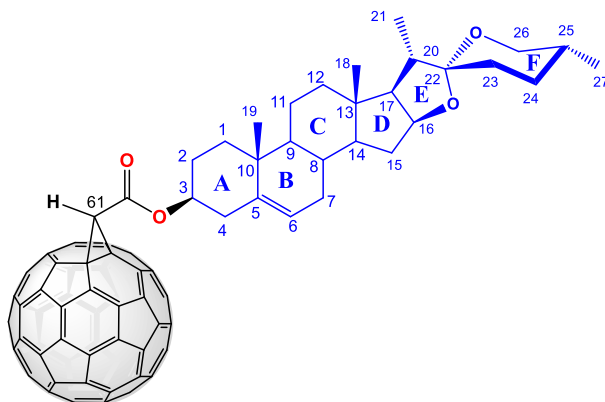
*Figure 10 Synthesized product **4** labeled H's and C's to indicate ^{1}H-NMR and ^{13}C-NMR signals.*

- **ATR-FTIR** (ν cm^{-1}): 2948, 2874, 1735, 1455, 1188, 1157, 980.
- **^{1}H-NMR** (700 MHz, CDCl3, δ ppm): 5,49 (m, 1H, H6), 4,97 (m, 1H, H3), 4,76 (s, 1H, H61), 4,43 (m, *J* = 8,7, 7,6, 6,5 Hz, 1H, H16), 3,48 (m, 1H, H26a), 3,39 (t, *J* = 11,0 Hz, 1H, H26b), 2,64 – 2,56 (m, 2H, H4), 2,15 (m, 1H, H12a), 2,07 – 1,95 (m, 3H, H1, H23a), 1,88 (m, 2H, H12b, H20), 1,80 (dd, *J* = 8,7, 6,7 Hz, 1H, H17), 1,77 (dt, *J* = 12,5, 3,4 Hz, 1H, H2), 1,68 (m, 2H, H7), 1,65-1,58 (m, 4H, H8, H11, H24, H25), 1,54 – 1,41 (m, 3H,

H2, H11, H24), 1,34 – 1,27 (m, 2H, H15), 1,24 – 1,19 (m, 1H, H23b), 1,18 – 1,14 (m, 1H, H14), 1,13 (s, 3H, H19), 1,04 (td, $J = 11,7, 4,9$ Hz, 1H, H9), 0,99 (d, $J = 7,0$ Hz, 3H, H21), 0,81 (s, 3H, H18), 0,80 (d, $J = 6,4$ Hz, 3H, H27).

- **^{13}C-NMR** (175 MHz, CDCl3, δ ppm): 165,93 (C=O), 146,03, 145,32, 145,24, 144,92, 143,87, 143,41, 143,10, 142,95, 142,36, 141,27, 141,06, 140,67, 148,51, 148,48, 146,03, 145,79, 145,32, 144,82, 144,10, 143,87, 143,41, 142,95, 142,23, 141,06, 140,67, 139,39 (C5), 123,19 (C6), 109,45 (C22), 80,94 (C16), 76,75 (C3), 70,87 (Csp^3 cyclopropane ring), 70,85 (Csp^3 cyclopropane ring), 67,01 (C26), 62,20 (C17), 56,57 (C14), 50,06 (C9), 41,77 (C20), 40,42 (C13), 39,87 (C2), 39,43 (C61 cyclopropane ring), 38,32 (C4), 37,15 (C1), 36,96 (C10), 32,23 (C23), 32,00 (C15), 31,55 (C8), 31,53 (C7), 30,45 (C25), 28,95 (C24), 28,10 (C12), 21,01 (C11), 19,58 (C19), 17,30 (C27), 16,47 (C18), 14,70 (C21).

- **MALDI-TOF** m/z: $[M+H]^+$ Calculated for $[C_{89}H_{43}O_4]^+$: 1176.29; Found: 1176.32

2.3. Computational approach

2.3.1. Geometry optimization and frequency calculations

The optimization was done after the initial structures involved in the reaction were drawn in Avogadro software. The structures were taken, and the calculation is run in ORCA until it converges to a minimum. In this way, since our molecules are composed of several atoms, we use the nonempirical Perdew–Burke–Ernzerhof (PBE) GGA because it allows us to perform the computational calculations at a moderate computational cost. The input used is composed of a functional (PBE), the dispersion corrector (D3BJ), an optimization method (OPT/FREQ), a basis set (6-31G), and an auxiliary basis set (def2/J). The overall procedure consists of two main steps: a) Optimization of the molecular geometry and b) Vibrational frequency calculations of the optimized structures. Thus, if all the vibrational frequencies calculated are positive, the structures with minimum energy locally were achieved.

In this way, all the structures in Figure 11 were individually optimized. It means to find a minimum geometry for **2**, protonated DBU (DBUH$^+$), **3**, resonance structures of galactose cation, DBU, and **4**. In addition, H_3O^+ and H_2O were also optimized.

16
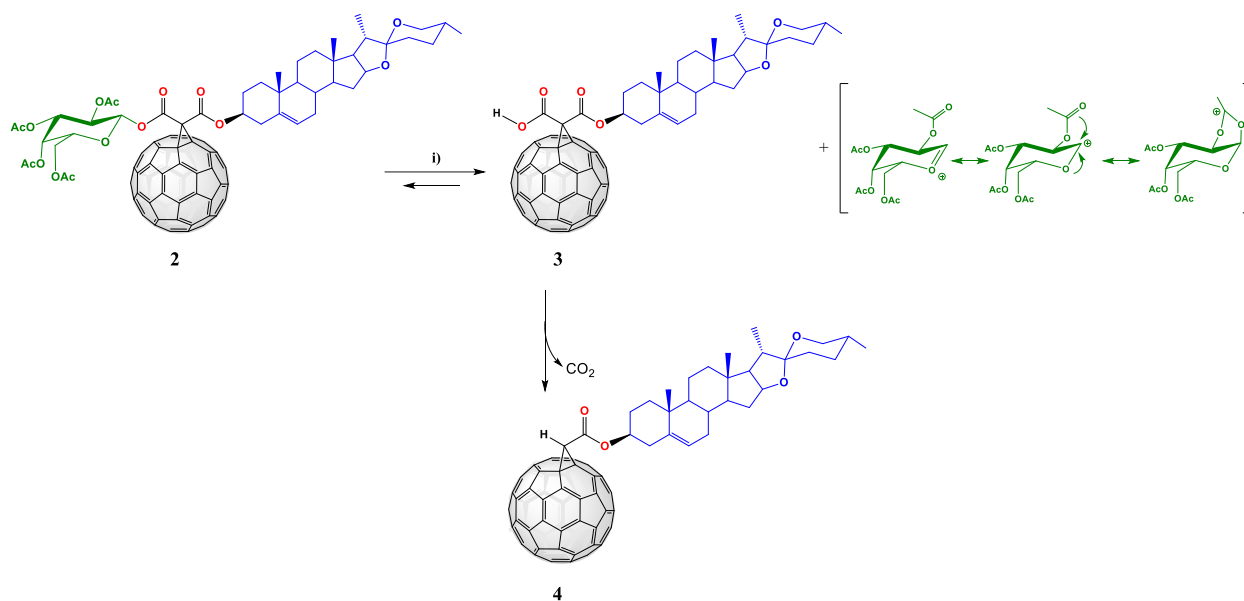
Figure 11 Reaction scheme showing all optimized molecular structures to generate the mechanism reaction. i) The hydrolysis could be assisted by DBUH$^+$ or H$_3$O$^+$.

2.3.2. The theoretical approach to the reaction: Mechanism Calculation

The mechanism analysis is considered since the temporary formation of the Bingel product 2. The reaction pathway study involved reagents, two transition states, one intermediary, and products. Thus, reagents (**2** and **DBUH$^+$** or **2** and **H$_3$O$^+$**), transition state 1 (**TS1**), intermediary (**INT**), transition state 2 (**TS2**), and products (**3**, **galactose cation**, and **DBU** or **H$_2$O**) were optimized. Once the mentioned structures were calculated, frequency calculations were run to verify that they corresponded to the desired structures. The input used to find minimum geometries was PBE D3BJ OPT (OptTS for transition states) 6-31G def2/J RIJCOSX. The same input was used to calculate vibrational frequencies but OPT was changed by FREQ keyword.

2.3.3. Transition States

Calculating the mechanism involves finding the minima and transition states of the molecules. This theoretical research calculated two transition states (**TS1**, **TS2**) and one intermediate (**INT**) based on the proposed mechanism. The TSs were calculated once the minimum structures corresponding to reagents and intermediate were obtained.

In this way, two processes were done to find TS1: a) a relaxed surface scan (geometry Scan) and b) the optimization (OptTS) with the scanned local maximum to find the TS1 related to the protonation of the carbonyl group. First, a relaxed surface scan from the optimized position of

reactives between a proton of the conjugated acid (DBUH$^+$ or H$_3$O$^+$) to the oxygen of the carbonyl group to be protonated until 1 Å was run. It involves the proton to be transferred of either DBUH$^+$ or H$_3$O$^+$ and the O of carbonyl group of the ester bonded the galactose. The distance of 1 Å was established based on some calculations executed to identify a close point to TS1. Then, the energy was plotted as a function of reaction coordinates, and the highest point on the curve was not at the peak of the curve but close to it. Consequently, a second relaxed surface scan was run from the previous highest point to 1 Å where it was obtained the local maximum. Second, we optimized (OptTS keyword used) this local maximum with two constraints to fix the distance of the transferred proton and avoid the free movement of atoms. The TS2 was found testing some distances until found the correct one and no constraints were necessary.

The ester hydrolysis's potential energy profiles were plotted using the final single point energies of the calculated structures in the gas phase. The keywords needed to run a relaxed surface scan are shown in image a from Figure 12. For instance, it means scanning the distance between atoms 135 and 179 from 1.703 Å to 1 Å in 10 steps. The keywords needed to include distance constraints are shown in image b from Figure 12. For example, it means a bond constraint between atoms 136 and 186 at a determined distance C.

```
a) %geom Scan                 b) %geom
   B 135 179 = 1.703, 1, 10      Constraints
   end                           {B 136 186 C}
   end                           end
                                 end
```

Figure 12 Keywords: a) to run a relaxed surface scan between atoms, and b) to include distance constraints.

3. Chapter III: Results and discussion

3.1. Synthesis of fullerene-steroid hybrid

61-(3β-O-carbetoxy-25R-spirost-5-en)methano[60]fullerene (**4**) was obtained through the cycloaddition reaction (Bingel-Hirsch methodology) between 3β-D-Galactopyranose, 2,3,4,6-tetraacetate malonate-25R-spirost-5-en (**1**) and C$_{60}$, as depicted in Figure 13. The acetate groups on the D-galactose are protective groups to avoid secondary reactions. Stoichiometric quantities

of compound 1 and fullerene were used. The cyclopropanation reaction was carried out at room temperature by mixing the fullerene with **1**, CBr$_4$, and DBU. After adding the DBU, a color change in reaction from deep purple to brown was observed which indicates the chemical transformation onto the C$_{60}$ molecule. In this way, it was produced the [6-6]-closed mono-adduct **4**. The reaction was followed by thin-layer chromatography (TLC), and after 90 minutes, it was completed. Then, the described isolation and purification (See Subsection 2.2) to obtain the final product. The synthesized conjugate **4** was purified by flash chromatography using CS$_2$ to elute the unreacted fullerene and then DCM to collect the mono-adduct **4**. After solvent evaporation, the exohedral product was obtained as a stable brown solid with a 50 % yield.
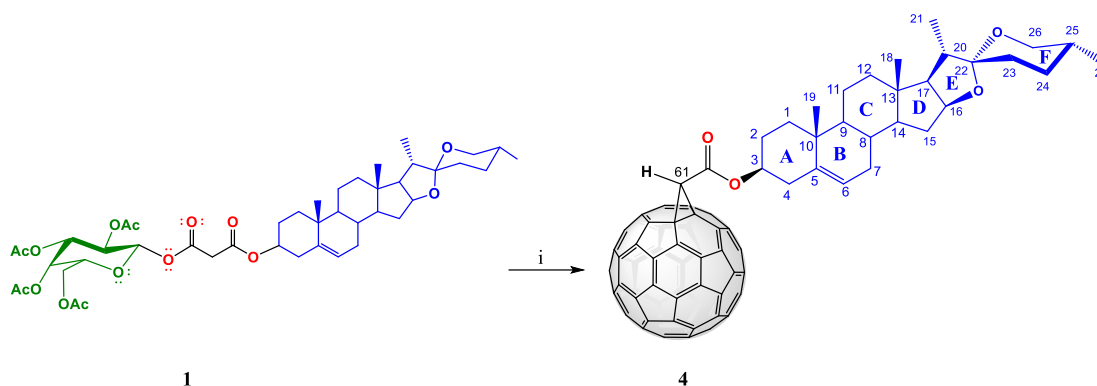
Figure 13 Synthesis of fullerene-steroid hybrid 4. i) C$_{60}$, CBr$_4$, DBU, toluene, room temperature, 90 minutes.

The chemical structure of the synthesized steroid-fullerene **4** was unambiguously corroborated by NMR, FTIR, and MALDI-TOF. According to the bibliography, there are no reports where fullerene is conjugated to D-galactose-diosgenin malonate or a steroid moiety-like compound **4**. Nevertheless, the research group of Suarez *et al.* has previously reported fullerenes conjugated with steroids[12,63,64].

The experimental and theoretical FTIR results are represented in Table 3 and Figure 14. The most important bands are summarized in Table 3 and were assigned based on the movement of functional groups seen in the calculated spectra. The signals corresponding to the symmetric and asymmetric CH$_3$ stretch are shown at 2948.39 and 2874.61 cm^{-1}. The peaks at 2926.18 and 2851.86 cm^{-1} are highlighted as belonging to symmetric and asymmetric CH$_2$ stretching, respectively, and the CH$_2$ bending was observed at 1430.1 cm^{-1}. The ester functional group was corroborated by the medium band stretching vibration appearing at 1735.36 cm^{-1}, corresponding

to the C=O and the signals at 1188.65 and 1157.02 cm^{-1} related to the C-O stretching. Finally, the characteristic band of organofullerene derivatives was observed at circa 730 cm^{-1}. A simulated FTIR spectrum of **4** was obtained using computational methods and compared to the experimental ones, as can be observed in Figure 14 and Table 3. It was appreciated that the accuracy of computed harmonic vibrational values is comparable with the experimental ones for a broad region of vibrational frequencies, highlighting those corresponding to the most important functional groups of **4**.

*Table 3 IR results for the experimental product **4***

IR bands for an experimental product		
Assignation	**Experimental wavenumber [cm^{-1}]**	**Theoretical wavenumber [cm^{-1}]**
C-H stretch (cyclopropane)	3228.32	3102.29
=C-H stretch	-	3078.98
-CH$_3$ asymmetric stretch	2948.93	3063.25
CH$_2$ asymmetric stretch	2926.18	3030.96
-CH$_3$ symmetric stretch	2874.61	2983.68
CH$_2$ symmetric stretch	2851.86	2964.77
C=O stretching	1735.36	1659.92
CH$_2$ scissoring	1455.44	1489.93
-CH$_3$ asymmetric bending	1376.12	1406.74
-CH$_3$ symmetric bending	1328.19	-
C-O stretch ester	1188.65, 1157.02	1193.35, 1173.68
C-O stretch ether	1100.38, 1050.20	987.19, 936.56
Organofullerene	738.81	723.17
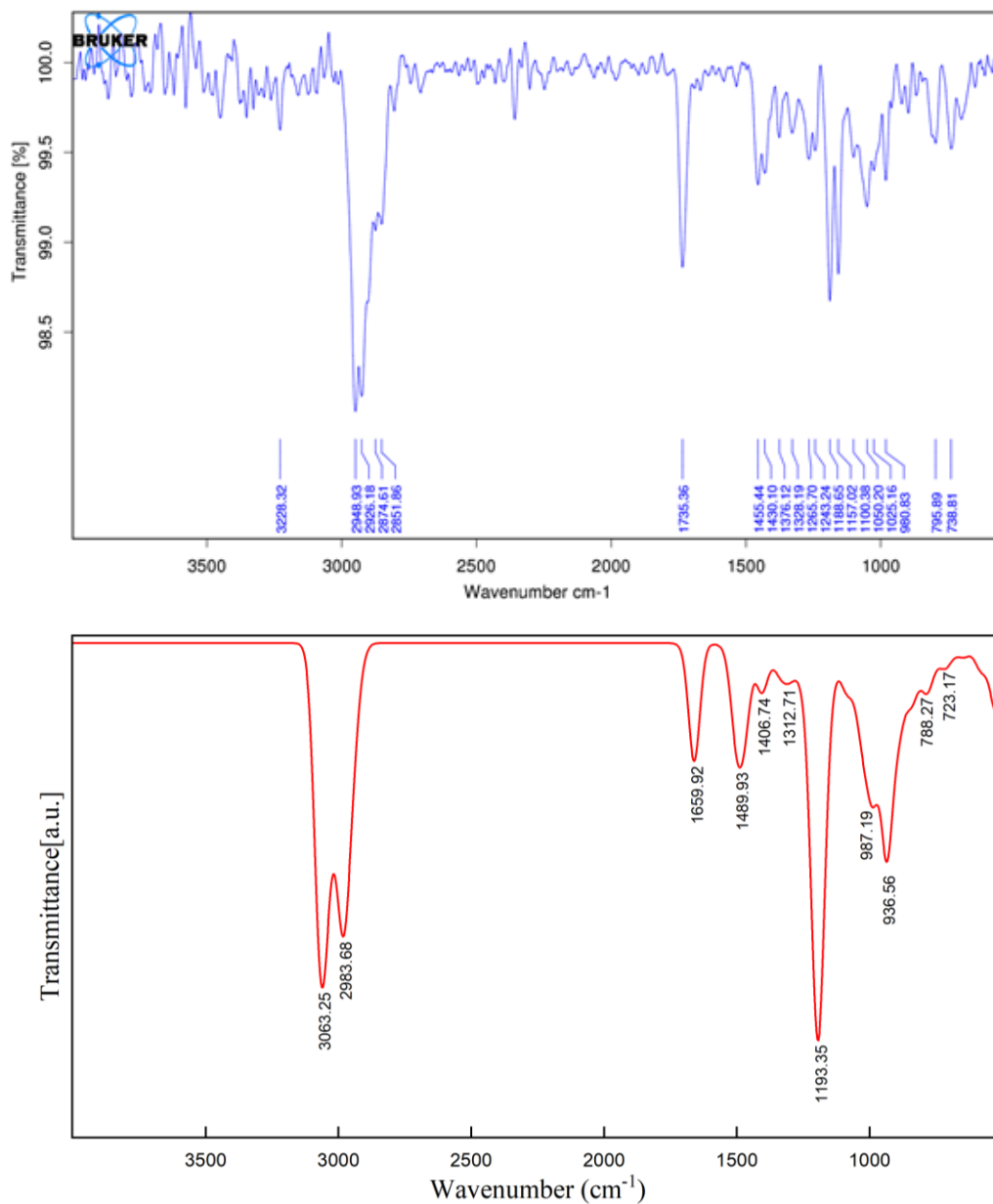
Figure 14 IR spectra for 4 blue for experimental and red for simulation.

NMR spectroscopy gives us information to verify the covalent link of malonate derivative **1** to fullerene. The NMR signals were similar to that of compounds previously reported by the same research group[12,23,64]. In the ^{1}H-NMR spectrum, which is shown in Figure 15, is not observed the methylene protons of the D-galactose-diosgenin malonate (**1**), which appear as a singlet at ca. $\delta \approx$ 3.3 ppm[63]. The critical signal indicating the absence of the D-galactose moiety is the presence of a singlet at $\delta = 4.76$ ppm assigned to the unique proton H61 of the cyclopropane ring. Moreover, the multiplet at $\delta = 5.49$ ppm is assigned to the proton H6 of ring B. The multiplet at 4.97 ppm

corresponds to the proton on C3 located at ring A, indicating the presence of the steroid moiety conjugated to the fullerene[63]. The other signals at the low field are those corresponding to the proton H16 and H26, bonded to C's close to oxygen, promoting the de-shielding signals at 4.43 and 3.48 ppm, respectively. Finally, the signals corresponding to the aliphatic H's of the steroid skeleton appear at the high field from 0.8 to 2.7 ppm.
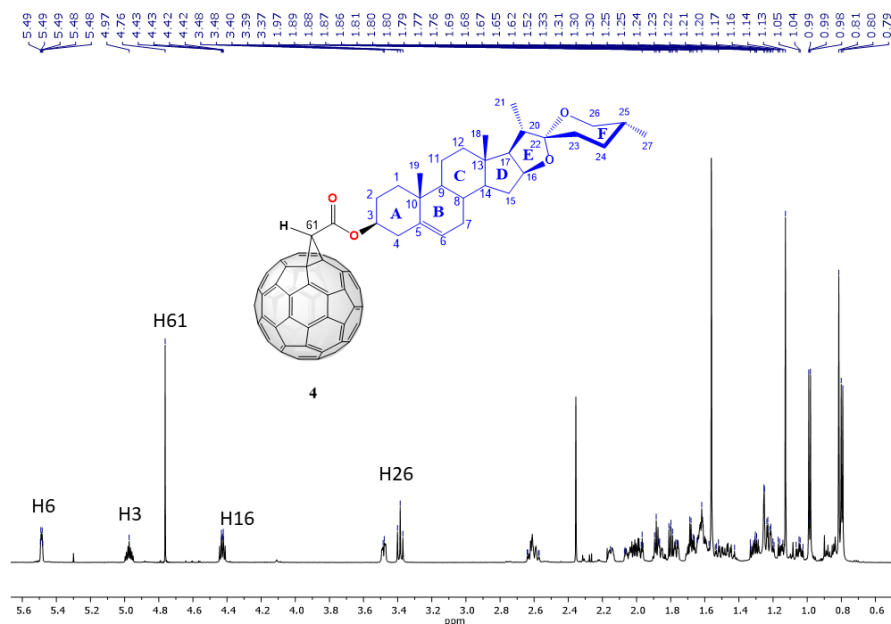
Figure 15 ^{1}H-NMR spectrum of compound 4

^{13}C-NMR spectrum of monoadduct **4**, observed in Figure 16, evidence the lack of symmetry in the fullerene conjugates because of the vast number of signals at the sp^2 carbon zone from 125 to 147 ppm. The signal at 165.93 ppm, was assigned to the unique carbonyl group present in the malonate fragment. The peaks detected at 139.39 and 123.19 ppm correspond to the unsaturated carbons C5 and C6 in ring B of the steroid moiety. The peak at 109.45 ppm was assigned to sp^3 C22, appearing at low-field because the two oxygen atoms link to this carbon. Furthermore, conjugate **4** showed the signal corresponding to C3 of ring A at 76.75 ppm. The other important at 70.87 and 70.85 ppm, which correspond to the 6,6-ring junction of both C$_{60}$ to the cyclopropane ring. Finally, the peak observed at 39.43 ppm was assigned to the carbon atom C61 closing the formed cyclopropane ring on the C$_{60}$.

22
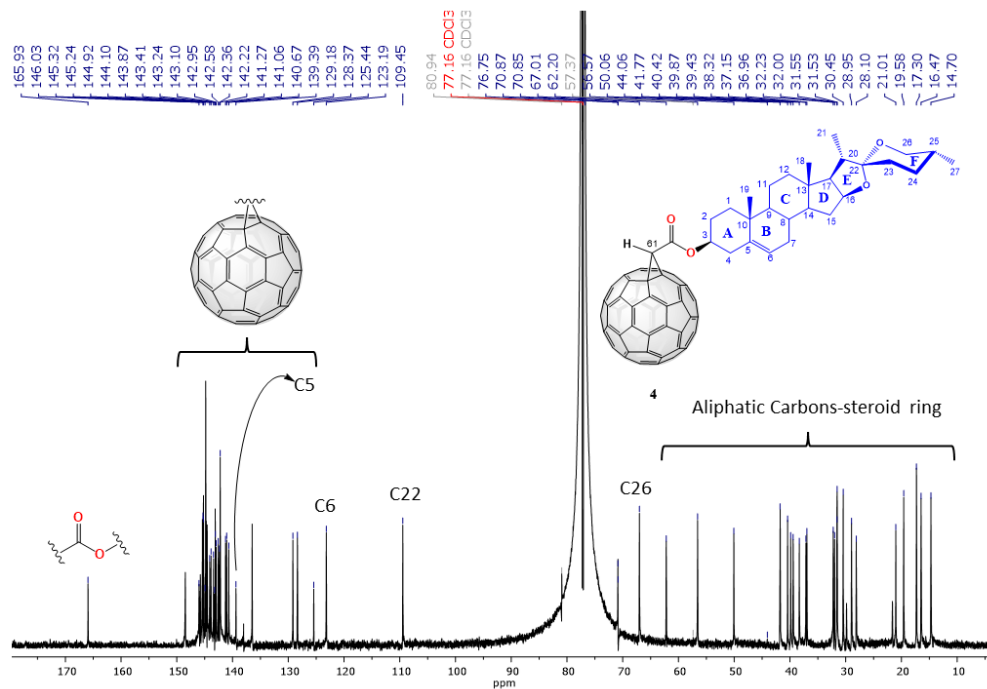
*Figure 16 ^{13}C-NMR spectrum of compound **4***

Figure 17 showed a peak at m/z 1176.32, corresponding to [M+H]$^+$.
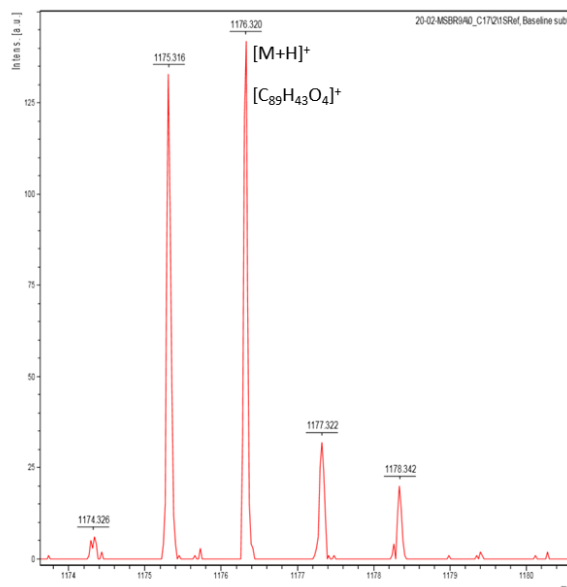
*Figure 17 MALDI-TOF spectrum of compound **4**.*

This unusual behavior observed in the previously described Bingel-Hirsch reaction has not been reported before. Figure 18 shows the reaction pattern proposed for the unexpected product formation, promoted by the early release of galactose cation.
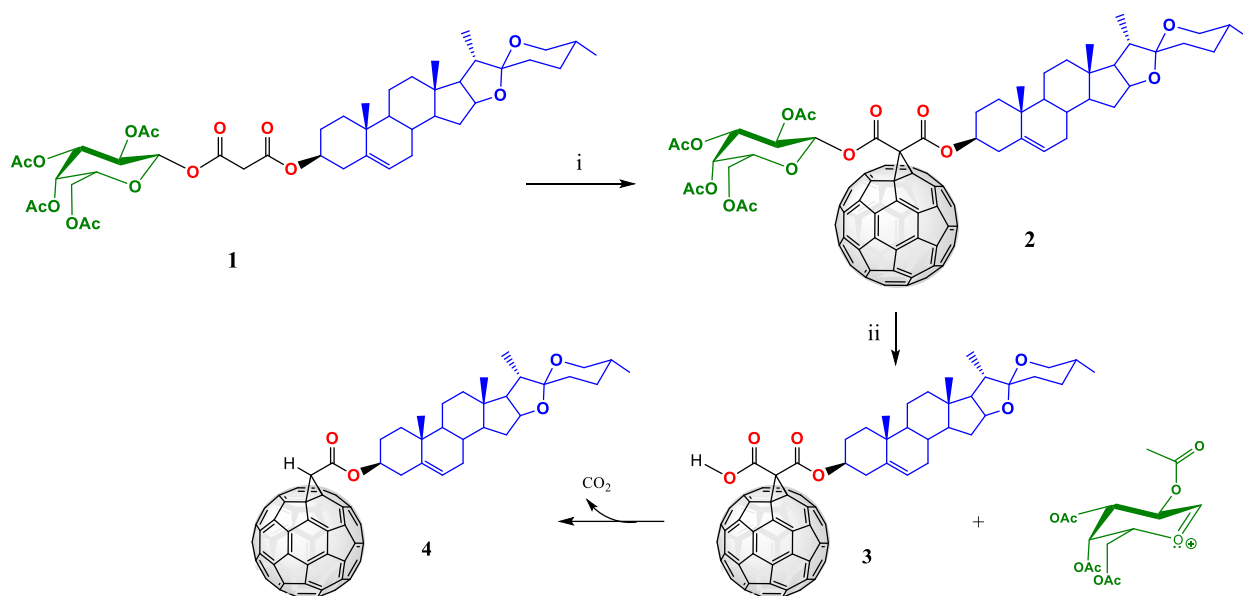
Figure 18 Scheme synthesis for the studied reaction. i) C_{60}, CBr_4, DBU, toluene, room temperature. ii) Hydrolysis could be assisted by $DBUH^+$ or H_3O^+.

With the experimental evidence, it is possible to postulate mechanisms for the described reaction.

3.2. Proposed Reaction Mechanism

For any proposed mechanism, it is essential to note that the $DBUH^+$ or H_3O^+ could assist the Bingel-Hirsch product's protonation and drive the subsequent release of D-galactose and the formation of carboxylic acid. It is crucial to consider that both molecules $DBUH^+$ and H_3O^+ are present in the reaction medium. In this way, two different reaction pathways would be possible considering two potential protonation sites in the ester function. It is reported that under proton enriched media ($DBUH^+$ and H_3O^+), the ester hydrolysis could occur via oxygen-carbonyl protonation, as represented in the proposed mechanism in Figure 19. However, we also presented the hydrolysis assisted via the oxygen-alkoxy group protonation of the ester as a possible reaction pathway, represented in Figure 20.

As is shown in Figure 19 for Mechanism I, if the carbonyl group is protonated, **2H-a** is generated from Bingel product **2**, and the mesomeric effect due to the adjacent alkoxy group promotes additional resonance structures **2H-b** and **2H-c**, proposing the D-galactose cation release in the last one **2H-c**. When the alkoxy group of the ester is protonated, as shown in Figure 20 for Mechanism II, the positive charge over the oxygen promotes the D-galactose cation release. In both proposed mechanisms, the galactose is liberated as a cation. The acetate group in the

24

equatorial position rotates and forms an additional resonance structure. A five-atom ring with carbon 1 of D-galactose and a tertiary carbocation is possible. This third resonance structure stabilizes the cation converting it into a good leaving group, classifying this effect as neighboring group participation. The highly stabilized cation release allowed us to propose that the described hydrolysis happens through an $A_{AL}1$ mechanism. For both proposed mechanisms, with the carboxylic acid **3** in hand, a typical decarboxylation occurs, and the final product **4** is generated.
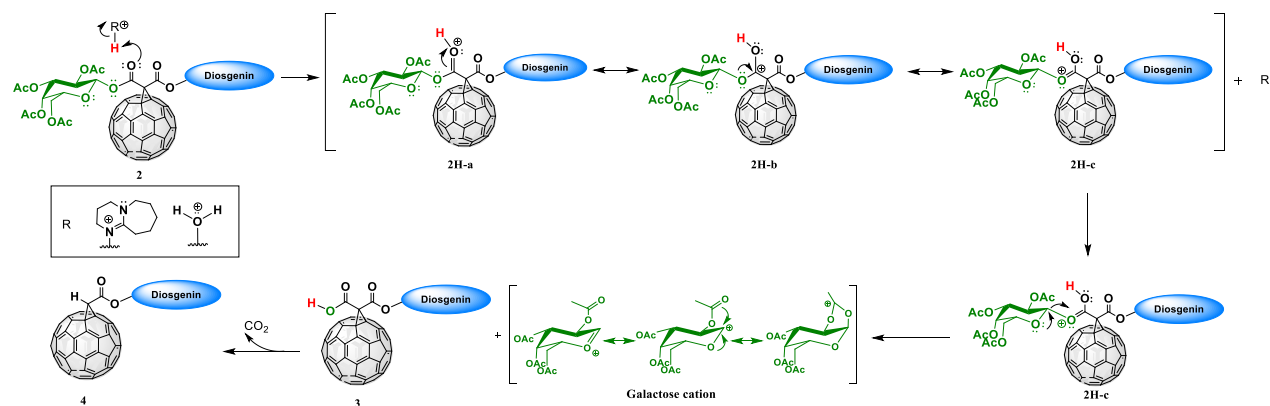
Figure 19 Proposed reaction mechanism I.
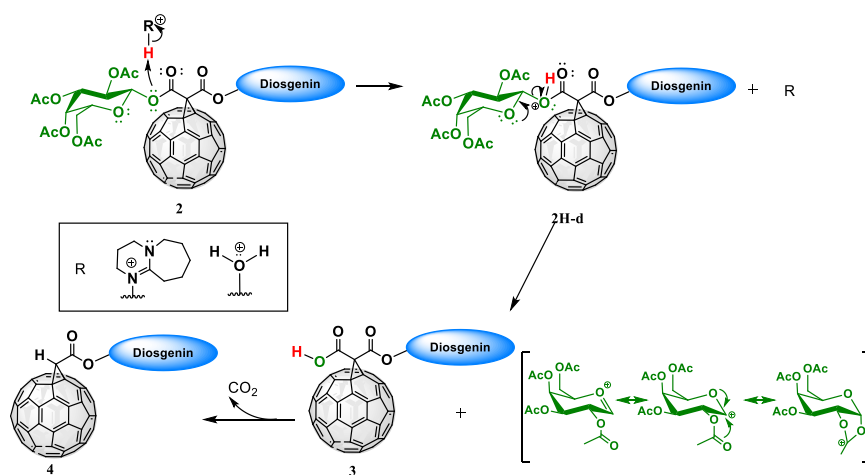
Figure 20 Proposed reaction mechanism II

Although both mechanisms I and II could be possible, chemical considerations would incline us towards the first proposal based on the stability conferred by the resonance of protonated species **2Ha-c**. When the carbonyl group of the ester is protonated, three resonance structures can contribute to the overall molecule stability. As a late transition state would be expected, the stabilization of this intermediate would lower the activation energy, making the protonation step easier. The mentioned resonance stabilization is not possible in Mechanism II.

25

3.3. Theoretical approach

To better understand the geometrical and electronic properties of the molecules involved, predict and compare some properties, and have a first approach to the reaction mechanism, a theoretical study was developed using density functional theory (DFT) and the semi-empirical method, Parametrical Model Number 3 (PM3).

3.4. Geometry optimization

All molecular structures involved in the galactose moiety released from **2** were calculated using the PBE (Perdew, Burke, and Ernzerhof) method and the 6-31G basis, and def2/J as an auxiliary basis set, affording the minimum energy conformations of compounds.

In this way, several conformations of compound **2** were assessed to select the most stable one to continue with the calculations for the mechanism reaction. The conformers resulting from orientation changes of the red highlighted oxygen atoms forming dihedral angle O = C···C=C on the Bingel hybrid structure **2** shown in Figure 21 were considered based on previous reports of similar systems[12,23,64].
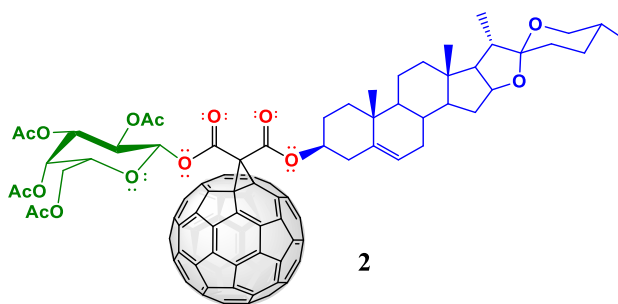
*Figure 21 Compound **2** highlights in red the dihedral angle C=O···C=O of the malonate unit.*

The calculated conformers for **2** are shown in Figure 22, and the obtained energies for the most stables **2C-a-e** are summarized in Table 4. The results shown in Table 4 indicate that **2C-a** conformer was the most stable. However, we can see that the difference in energy between conformations is around 7 kcal/mol. The conformations energy difference is due to the orientation of both substituents in the malonate unit where they found an optimal position to minimize steric hindrance. Furthermore, we observed hydrogen bonds between oxygen atoms of the galactose ring (O1) and the acetate group (O2 and O3) hydrogen atoms of rings A (H1) and B(H2) which are represented in Figure 23. Calculations predicted a tendency to a relative s-trans

conformation of the carbonyl groups of the malonate unit when the fullerene aggregate is present. These results agree with those previously reported by Suárez research group [12,23,64].
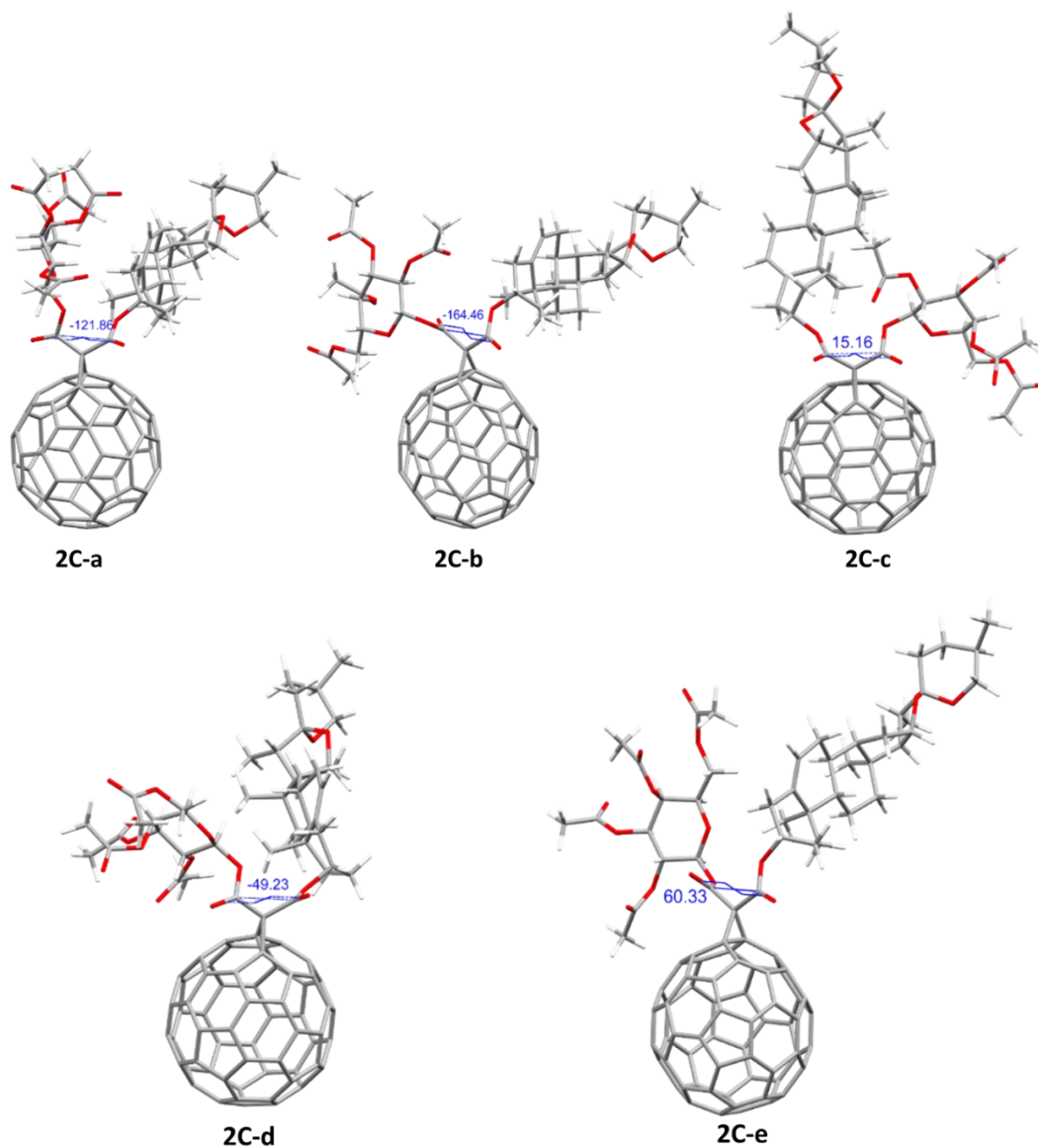
*Figure 22 Different configurations calculated for compound **2** obtained by the DFT-PBE method using a 6-31G basis set. Dihedrals' angles are highlighted in blue and expressed in degree (°).*

*Table 4 Energy of **2C-a-e** conformer*

	Energy [E_h]	Energy [kcal/mol]	Difference [kcal/mol]
2C-a	-5120.501	-3213114.074	0.000
2C-b	-5120.489	-3213106.559	7.515
2C-c	-5120.486	-3213105.062	9.012
2C-d	-5120.489	-3213106.633	7.441
2C-e	-5120.488	-3213106.263	7.810
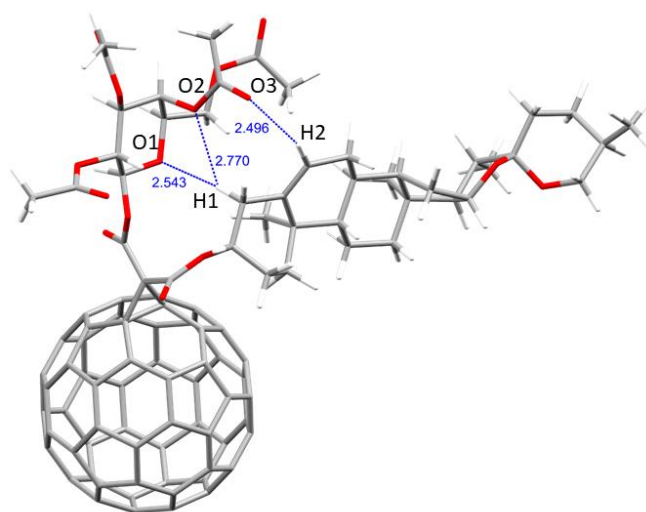
*Figure 23 Molecular geometry of **2C-a** showing hydrogen bonds in blue. Distances are given in Å.*

The conformer **2C-a** was selected for further calculations, considering it is an s-trans conformation and has lower energy implying higher stability. All the calculated vibrational frequencies are positive, corroborating that these structures correspond to a minimum.

$DBUH^+$ and H_3O^+ were calculated, and their optimized structures are shown in Figure 24.

Protonated 1,8-diazabiciclo[5.4.0]undeca-7-eno
(DBUH⁺)

Hydronium cation (H_3O^+)
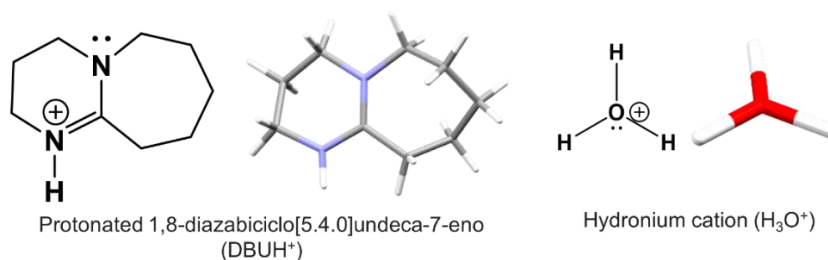
Figure 24 Optimized molecular geometry of DBUH⁺ and H₃O⁺ obtained applying the DFT-PBE method using 6-31G basis set.

Moreover, the structures of hydrolysis products **3**, D-galactose cation, and DBU were calculated, and the optimized structures are shown in Figure 25.
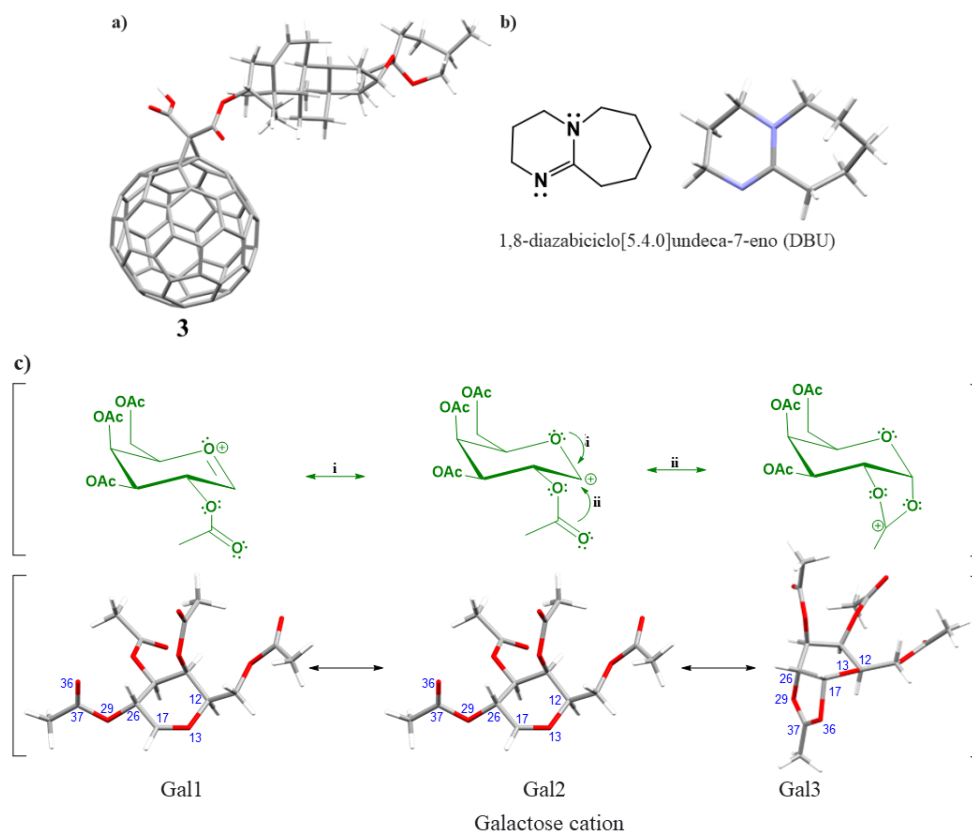
Figure 25 Optimized a) 3 b) DBU and c) resonance structures for D-galactose cation. From left to right, Gal1, Gal2, and Gal3 were obtained by the DFT-PBE method using a 6-31G basis set.

As was expected and confirmed by the calculated energies expressed in Table 5, the most stable resonance structure was Gal3 because of the tertiary carbocation and a five-member ring formation between the vicinal acetate group and C1 of galactose (neighboring group effect). Nevertheless, there is no remarkable difference in energy between Gal1 and Gal2, which means that these structures contribute similarly to the resonance hybrid. The obtained bond distances for the three resonance structures Gal1-3 also confirm the structural similarities between Gal1 and Gal2, as shown in Table 6.

*Table 5 Energy for resonance structures of Galactose cation (**Gal1-3**)*

	Energy [E_h]	Energy [kcal/mol]	Difference [kcal/mol]
Gal1	-1219.984	-765540.104	9.174
Gal2	-1219.985	-765540.393	8.885
Gal3	-1219.999	-765549.278	0.000

Atoms	Gal1	Gal2	Gal3
	Distances Å		
17-13	1.301	1.300	1.342
13-12	1.559	1.561	1.517
26-29	1.465	1.465	1.524
29-37	1.436	1.436	1.349
37-36	1.239	1.238	1.297
36-17	-	-	1.792

As was mentioned above, experimental evidence indicates that the expected Bingel-Hirsch product **2** suffers hydrolysis under proton enricher media to **3**, followed by decarboxylation, which allows the formation of **4**. The final product **4** was also calculated, and the optimized structure is shown in Figure 26. The observed difference in ring A conformation could be related to forming two H bonds with the right distances and angle[65]. The first between H3 and the carbonyl group of malonate with a length of 2.479 Å and 94.32° C3-H3···O angle. The second one is between equatorial H4 and the carbonyl group of malonate with a distance of 2.676 Å and 91.28° C4-H4 angle.
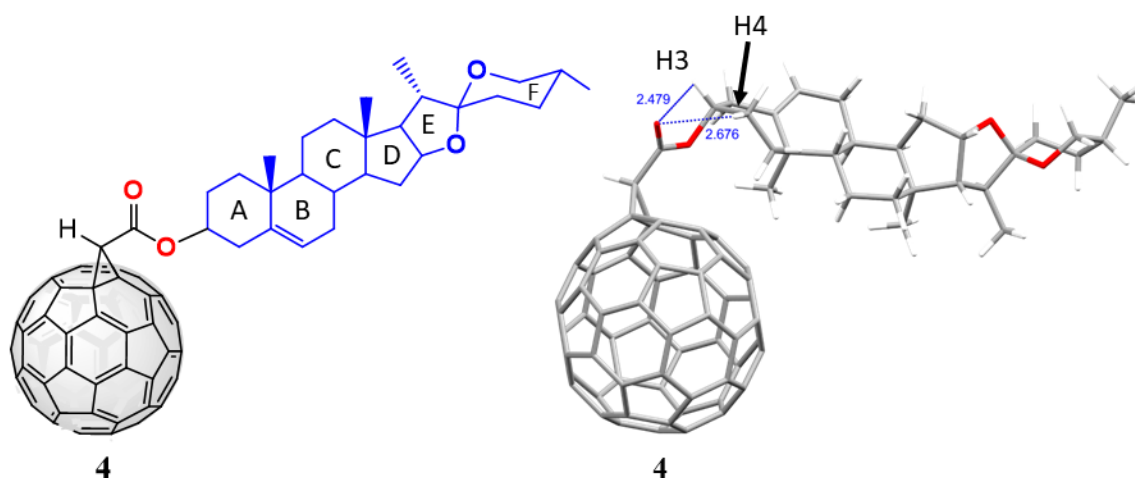
*Figure 26 Optimized molecular geometry of **4** obtained by the DFT-PBE method using 6-31G basis set. Bond distances are given in Å.*

Additional properties were calculated for **2** and **4** to predict the intramolecular and intermolecular electrostatic interactions, as shown in Table 7, to analyze how the structural modification due to the hydrolysis changes the specific properties such as the capacity to penetrate biological membranes, lipophilicity, and molecules polarity. All predicted results were consistent with the structural analysis of both compounds **2** and **4**.

*Table 7 Theoretical physicochemical parameters calculated for the expected Bingel-Hirsch product **2** and Final product **4***

Property	Compound	
	Bingel-Hirsch product (2)	**Final product (4)**
Volume Å^3]^a	1296	950.8
SASA [Å^2]^b	1331.07	1026.46
TPSA [Å^2]^c	47.92	44.76
Hy^d	-6.26	-6.26
Dipole moment [D]^e	2.55	2.93
logP^f	13.65	22.34
Polarizability [Å^3]^g	1024.37	812.63

[a] Total volume calculated in Chimera 1.16 using MSMS library for surface generation.
[b] Solvent-accessible surface area calculated by FreeSASA2.0.3 with Lee and Richards algorithm.
[c] Topological polar surface area calculated by BioTriangle web server.
[d] Hydrophilic index obtained by BioTriangle web server.
[e] Dipole moment retrieved from DFT calculation.
[f] Predicted octanol/water partition coefficient (lipophilicity) using XLOGPv3.2.2.
[g] Polarizability predicted with single point energy calculation using PBE functional and 6-31G basis set.

The solvent-accessible surface area (SASA) is the molecule surface available to interact with solvent molecules[66,67]. The chemical modification of C_{60} to a diosgenin-fullerene hybrid causes an increase in this measurement. It indicates a higher probability of 4 to interact with target molecules. The variation of SASA is an indirect indicator of the C_{60} as a K^+ channel blocker and hydrophobicity[63,68].

The topological surface area (TPSA) is defined as the sum of surfaces of polar atoms in a molecule. Palm *et al.*[69] indicate a correlation between TPSA value and its capacity to penetrate cell membranes, establishing that those molecules with TPSA values lower than 60 Å^2 can be absorbed easily, while values greater than 140 Å^2 results in not easy penetration of the cell membrane. Both analyzed compounds **2** and **4** showed TPSA values lower than the set threshold of 60 Å^2, concluding that both may act as potential biological membrane spanners. Therefore, the spontaneous hydrolysis of **2** and the subsequent decarboxylation don't affect the final product's ability to cross biological membranes.

The partition coefficient (P) is a physicochemical parameter related to the lipophilicity degree of analyzed compounds. It indicates the relative solubility of a determined substance in a mixture of two immiscible phases at a specific temperature. The predicted logP$_{ow}$ suggests that both compounds have high lipophilicity. Nevertheless, **2** (logP$_{ow}$=13.65) is less hydrophobic than

compound 4 (logP$_{ow}$ =22.34), consistent with the malonate and the sugar moieties in **2**. These values might indicate a tendency to form aggregates in aqueous media for this type of molecule, as reported for C$_{60}$ and their derivatives[12,63].

The dipole moment is defined by a sum over the net charge and the first moment of every atom in a molecule. In this regard, this property expressed the polar character or polarity of the molecules.[70] The similar values of the predicted dipole moment of **2** and **4** indicated that both are polar compared to the C$_{60}$. The dipole moment for **4** was slightly higher than the property for **2**.

The polarizability would be defined as a pivotal molecular property that can control the molecules' induction and dispersion forces. As shown in Table 7, the predicted polarizability could be considered higher than those expected and reported for pristine C$_{60}$[71]. Hydrolysis and decarboxylation in **2** reduced the polarizability. These values support the idea that electronic interactions must be considered for developing chemical-biological interactions.

In addition, it was calculated the molecular orbitals of compound 4 represented in Figure 27 using the DFT-PBE at 6-31G level of theory. The lowest unoccupied molecular orbitals (LUMO) are located specifically on the fullerene core and the electron density of the highest occupied molecular orbitals (HOMO) on some rings of the steroid skeleton. The calculated LUMO and HOMO energy values are -3.887 eV and -5.350 eV, respectively. A band gap of 1.47 eV has been predicted for compound 4. These values are in agreement with literature[12,63] for similar compounds.
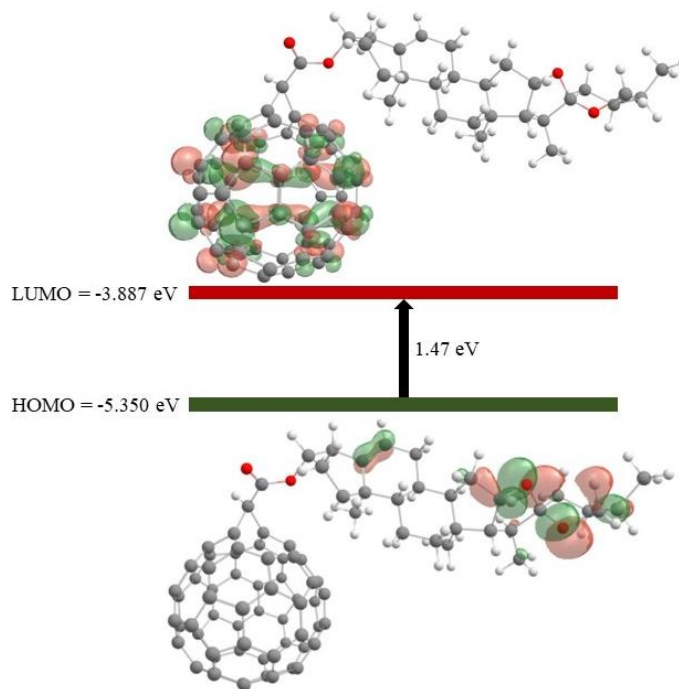
Figure 27 Molecular orbital diagram and calculated HOMO-LUMO energy level for compound 4 using DFT method at the PBE-6-31G level of theory in the gas phase.

Moreover, it was calculated the molecular electrostatic potential map (EPM) to analyze the electrostatic potential distribution of hybrid **4** represented in Figure 28. The EPM indicates that diosgenin covalently connected to fullerene modifies the electrostatic potential distribution resulting in three different colored regions. In this way, the red zone illustrated the oxygen atoms present in the carbonyl and ether groups and represented a negative density site. The blue zones indicated the positive areas of the steroid moiety related to the presence of the hydrogen atoms. In addition, the green zone of the hybrid means no representative charge separation, which indicates the lipophilicity of the molecule. In contrast, the reported EPM of fullerene is completely green colored[72], showing its high lipophilicity. As expected, the steroid molecule influences the electronic properties of the fullerene structure.
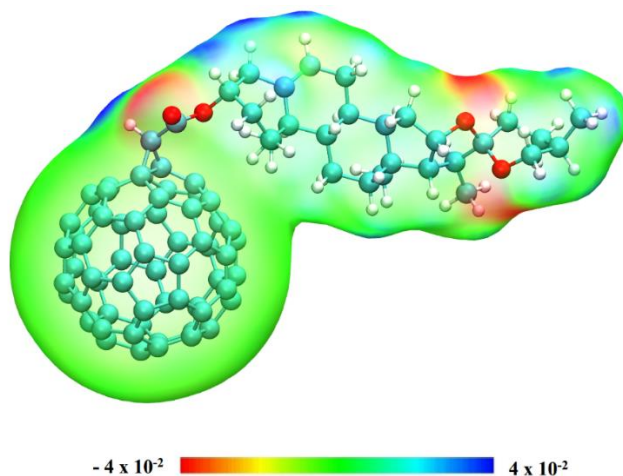
3.5. The theoretical approach to the reaction mechanism

The reaction profile was computed by locating the possible transition states (**TSs**) involved in forming the final product **4**, to deepen in the most feasible mechanism that explained the unusual behavior (hydrolysis and subsequent decarboxylation) observed for the compound **2**. Although two reaction pathways could be possible, the Mechanism I, shown in Figure 19, would be the favored promoted by the protonated specie resonance (**2Ha-c**), and chosen to carry out a first theoretical approach.

DFT methods have been considered the most accurate for calculating mechanism reactions; nevertheless, semi-empirical methods were considered more convenient due to our system's size composed of 207 atoms. The input used for optimization was PM3 OPT (OptTS for transition states) for minimum configurations; a relaxed surface scan was used to determine the transition states. It was necessary to establish constraints between atoms to avoid free atom movements. In addition, vibrational frequencies were calculated to verify if those structures corresponded to the right ones. The input used to calculate vibrational frequencies was PM3 FREQ.

As was mentioned above, the results and reaction conditions suggest that ester hydrolysis is assisted by protonated DBU (DBUH$^+$) or hydronium cation (H$_3$O$^+$). Therefore, the theoretical approach to both mentioned reaction pathways was carried out.

34

3.5.1. DBUH+-assisted galactose-malonate-diosgenin (2) hydrolysis

The first step for the more plausible mechanism implies the DBUH+- assisted protonation of carbonyl group close to galactose moiety. Thus, the DBUH+ and **2** were calculated together, as is shown in Figure 29, to find the optimal position between DBUH+ and **2**, allowing the optimal carbonyl protonation. Moreover, the main atoms involved in the protonation and breaking of the ester bond are labeled in Figure 29, and their calculated distances are summarized in Table 8.
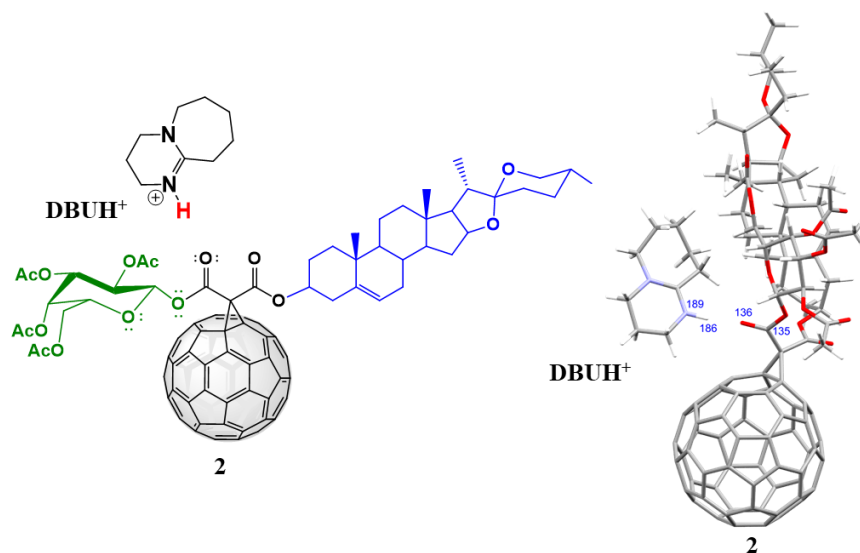
*Figure 29 Optimal disposition of reagents involved in the first step for the postulated Mechanism I, DBUH+ and Bingel-Hirsch product **2***

With the optimal reagents layout in hand, the first transition of the Mechanism I (**TS1**) was calculated by carrying out two relaxed surface scans of the distance between H-186 and O-136. The first one was from 1.802 to 1 Å in 10 steps. A near point to the maximum point was obtained, but it was not located on the top of the curve to establish the TS. Despite this, we used the first scan to select that point before the maximum distance, and a second relaxed surface scan from 1.267 to 1 Å in 10 steps was run, allowing us to obtain the maximum point at 1.148 Å. Then the OptTS calculation was carried out to get the **TS1** represented in Figure 30, in which the crucial atoms are marked out. For the OptTS calculation, we did not apply constraints. The main distances obtained from the calculated TS1 are collected in Table 8.
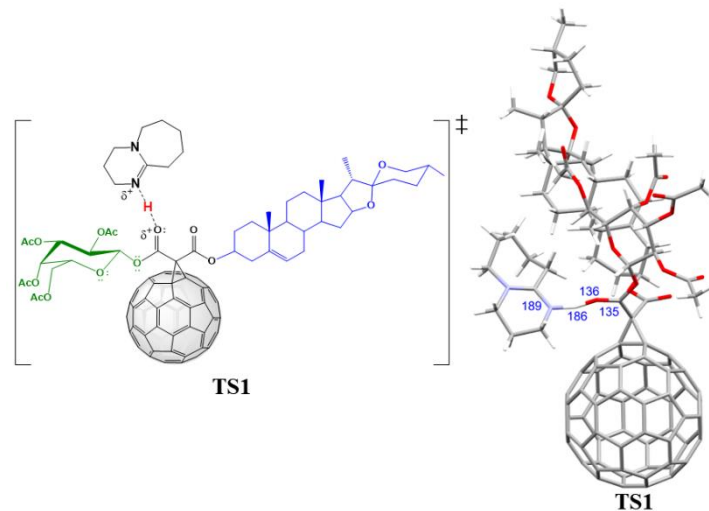
*Figure 30 Predicted **TS1** corresponding to step 1 for the postulated Mechanism I between DBUH⁺ and Bingel-Hirsch product **2**.*

The predicted **TS1** allowed to arrive at the intermediate **INT** where the proton was abstracted by the carbonyl group of the malonate moiety close to the galactose. The positive charge generated over the protonated carbonyl is delocalized upon O-C-O bonds, as was described by the resonance structures **2Ha-c** shown in Figure 21. The optimized structure for **INT** is represented in Figure 31, highlighting the mainly involved atoms. The main distances are compiled in Table 8.
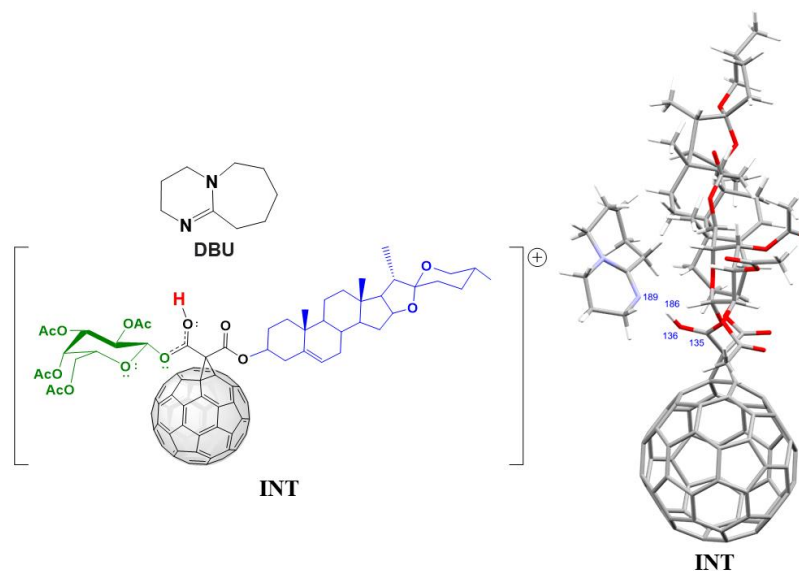
*Figure 31 Predicted **INT** corresponding to step 1 of the postulated Mechanism I between DBUH⁺ and Bingel-Hirsch product **2**.*

As was described in Figure 19, the second step of Mechanism I involve the concerted release of galactose cation and the carboxylic acid **3** formation. The transition state (**TS2**) corresponding to this step was calculated, and the optimized structure is represented in Figure 32. It was not necessary to use constraints to optimize **TS2**. The main distances are summarized in Table 8.
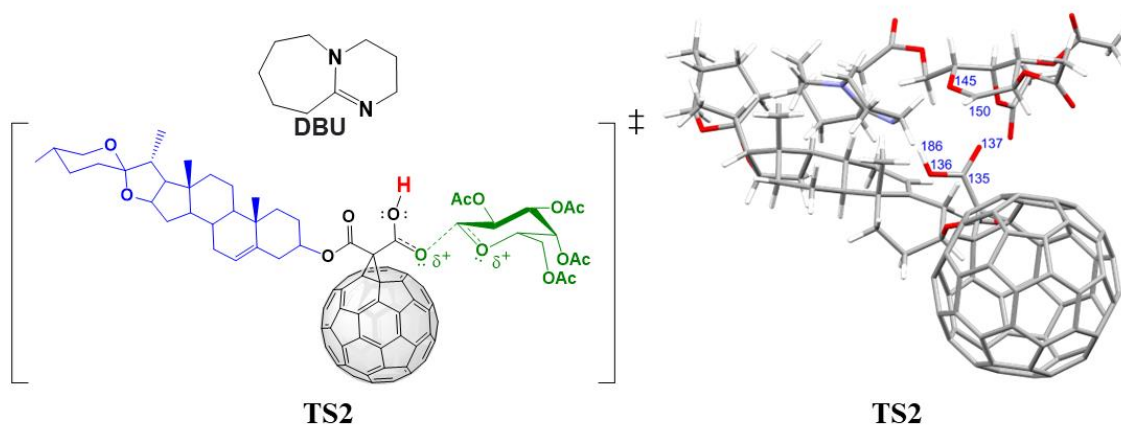
*Figure 32 Predicted **TS2** for step 2 of postulated DBUH[+]-assisted Mechanism I related to the concerted release of galactose cation and carboxylic acid formation.*

Finally, the carboxylic acid **3**, galactose cation and DBU are calculated as hydrolysis products. In this way, galactose adopts a cationic structure stabilized by their resonance structures **Gal1-3**, shown in Figure 25. The most stable resonance structure should be **Gal3**, conferring stability to the products, as pointed out before. **Gal3** was calculated, corroborating that this bicyclic carbocation stabilizes the products, represented in Figure 33. The main distances are collected in Table 8.
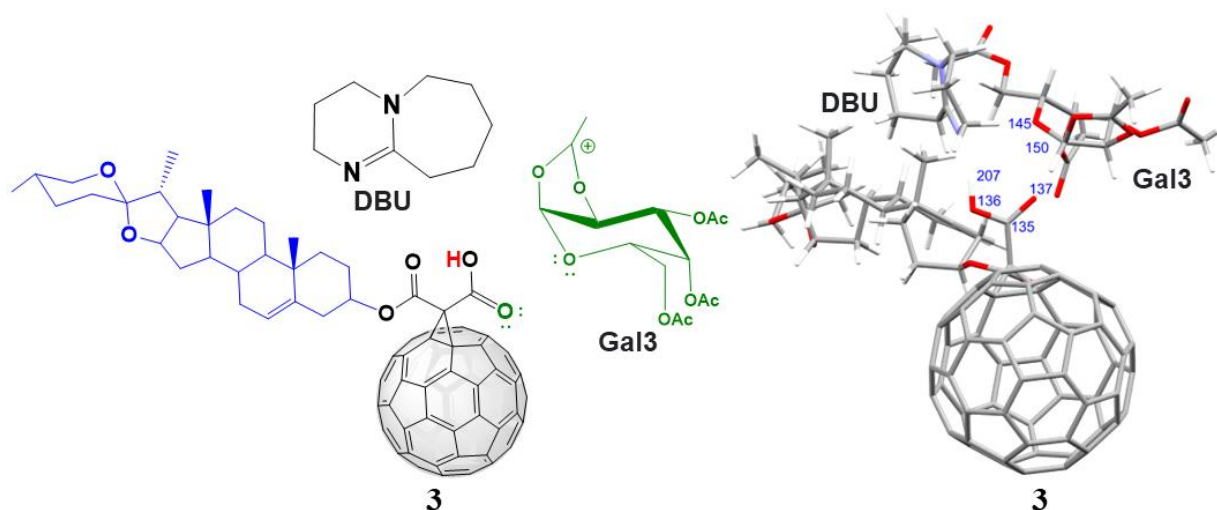
*Figure 33 Predicted hydrolysis products **3**, **Gal3**, and **DBU** for the postulated Mechanism I.*

37

Table 8 Distances between the atoms involved in the DBUH⁺-assisted hydrolysis of 2

# Atoms	Reactants	TS1	INT	TS2	Products
			Distances Å		
189-186	1.015	1.369	1.624	1.739	1.762
186-136	1.802	1.162	1.022	0.986	0.981
136-135	1.219	1.248	1.27	1.309	1.323
135-137	1.355	1.331	1.319	1.249	1.231
137-150	1.420	1.434	1.439	1.976	2.84
150-145	1.407	1.404	1.401	1.296	1.357

Once the molecular structures conforming to the Mechanism I had been optimized individually, the vibrational frequencies were searched.

Usually, DFT methods lead to positive frequencies for minimum or one negative frequency for transition states; however, the mentioned behavior was not strictly observed because of semi-empirical methods. Small negative frequencies inferior to -50 cm^{-1} were obtained for minimum structures and below -100 cm^{-1} for transition states. The significant negative frequency of **TS1** was -1418.09 cm$^{-1,}$ which corresponds to the transference of a proton occurs. This value agrees with the literature for a proton transfer employing semi-empirical methods[73] and also at the DFT B3LYP/aug-cc-pvtz level of theory[74]. The negative frequency calculated for **TS2** was -149.41 cm^{-1} which corresponds to the breaking of the ester bond and the formation of a carboxyl group of acid. This value agrees with the literature for breaking the ester bond and formation of the new carbonyl group[75].

The potential energy diagram (PED) for the DBUH⁺ - assisted hydrolysis of **2** was calculated in vacuo at the PM3 level and shown in Figure 34. According to the calculated results, the mechanism I follows a bimodal PED in the gas phase. The reaction seems to be endothermic (ΔH = 18.5 kcal/mol), with two steps; each has its transition states **TS1** and **TS2**, respectively. The rate-limiting step was the first one, with a theoretical activation free energy of 24.20 kcal/mol, and the second step comprised lower activation free energy of 13,06 kcal/mol. This process is not thermodynamically favored (ΔG = 17.91 kcal/mol); a positive ΔG indicates a not spontaneous reaction. The relative energies, enthalpies, and Gibbs free energies are summarized in Table 9.
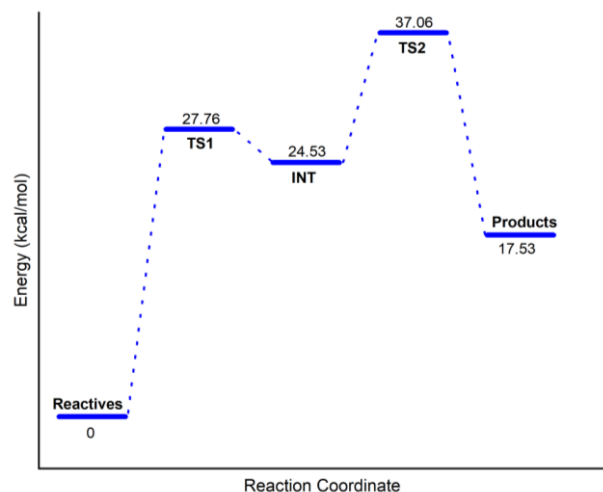
*Figure 34 Computed potential energy diagram (PED) for DBUH⁺-assisted hydrolysis of **2** in gas phase at PM3 level.*

*Table 9 Relative energies (ΔE), enthalpies (ΔH) and free energies (ΔG) of optimized DBUH⁺-assisted hydrolysis of **2** in the gas phase at PM3 level. All the values are reported in kcal/mol.*

	Starting reagents	TS1	INT	TS2	Products
kcal/mol			**PM3**		
ΔE	0.00	27.76	24.53	37.06	17.53
ΔH	0.00	23.50	23.89	35.94	18.50
ΔG	0.00	24.20	23.55	36.61	17.91

As was described before, the proton-enriched media to promote the hydrolysis of **2** can be provided by DBUH⁺ or H_3O^+. A similar theoretical study was carried out but replaced the DBUH⁺ with H_3O^+.

3.5.2. H_3O^+-assisted galactose-malonate-diosgenin (2) hydrolysis

The Mechanism I described in Figure 19 was studied, but H_3O^+ was used as the proton donor in place of DBUH⁺. Like the previously described process, the optimal position to promote the carbonyl protonation between **2** and H_3O^+ was calculated, and the optimized structures are shown in Figure 35. Moreover, the main atoms involved in the protonation and breaking of the ester bond are labeled in Figure 35, and the main distances are summarized in Table 10.
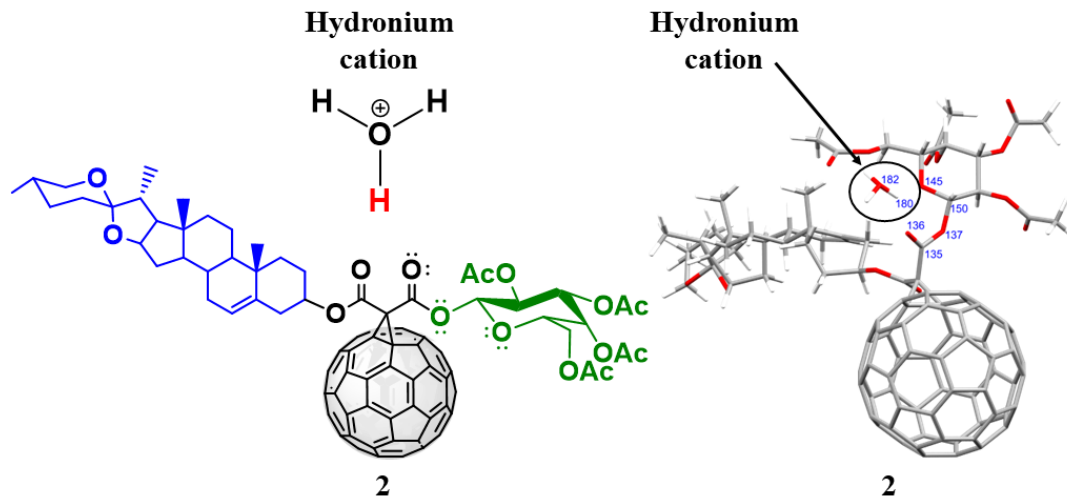
Figure 35 Optimal disposition of reagents involved in the first step for the postulated Mechanism I, H_3O^+ and Bingel-Hirsch product 2.

Once the disposition of starting reagents, **2** and H_3O^+, was optimized, the transition state of the first step, **TS1** was calculated. The predicted **TS1** is presented in Figure 36. Two geometry scans between the H_3O^+ and the carbonyl group were run. Despite the maximum point was not obtained with the first relaxed surface scan from 1.703 to 1 Å, it helped to have a smaller range to run a second relaxed surface scan from 1.391 to 1 Å. The last relaxed surface scan threw the maximum point at 1.262 Å. Then, we ran the optimization using two bond constraints between atoms numbered 182(O from H_3O^+)-180(H^+ from H_3O^+ to be transferred) and 180(H^+ from H_3O^+ to be transferred)-136(O of the carbonyl to be protonated) highlighted in Figure 36, at 1.297 and 1.262 Å, respectively. The constraints were necessary to keep a fixed position where calculate the corresponding **TS1**. Without restrictions, the optimization was carried out, but atoms moved out of the desired position. The main distances are collected in Table 10.
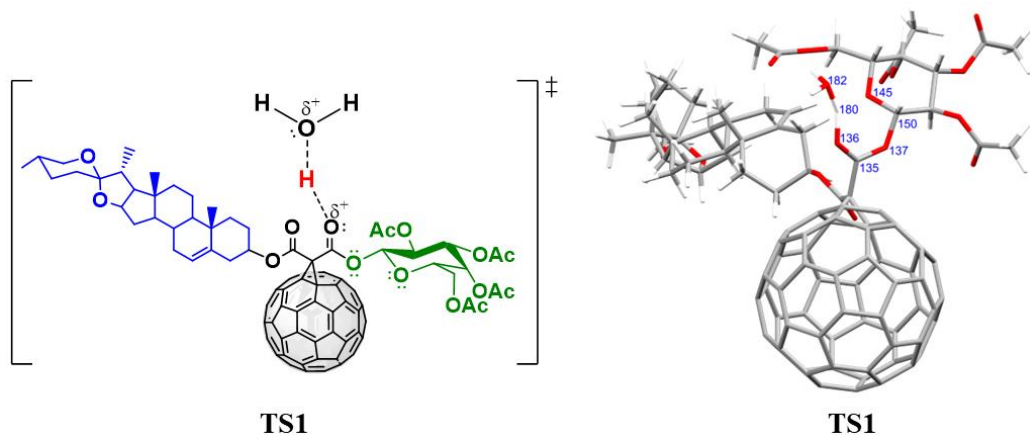
*Figure 36 Predicted **TS1** corresponding to step 1 for the postulated Mechanism I between H_3O^+ and Bingel-Hirsch product **2***

Then, the corresponding intermediate (**INT**) was calculated. The proton from hydronium cation is wholly transferred to the carbonyl group, and the positive charge generated is delocalized over the carbonyl and alkoxy group as shown in Figure 37. As was mentioned before, the delocalization of the positive charge on **INT**, which could be explained using resonance, stabilizes the intermediate. The optimized molecular geometry of **INT** is represented in Figure 37.
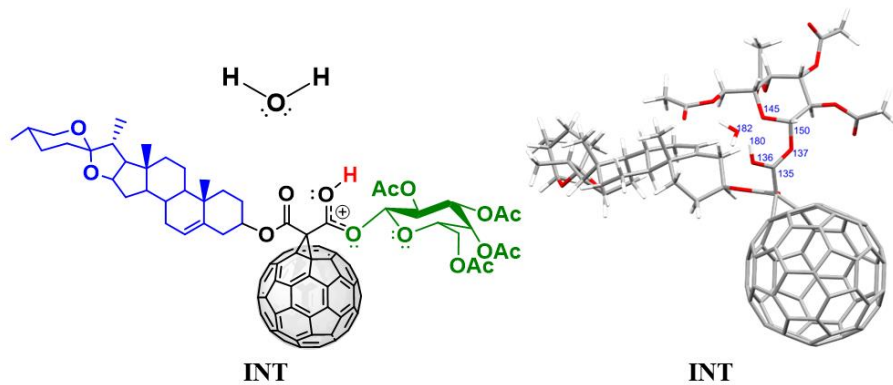
*Figure 37 Predicted **INT** corresponding to step 1 of the postulated Mechanism I between H_3O^+ and Bingel-Hirsch product **2**.*

The next step involves the coordinated Galactose cation release and carboxylic acid formation. The transition state **TS2** was calculated, and optimized structural geometry is shown in Figure 38. In the predicted **TS2,** the positive charge is delocalized toward the pyranose oxygen in the Galactose scaffold, promoting the subsequent sugar cation release as a good leaving group.
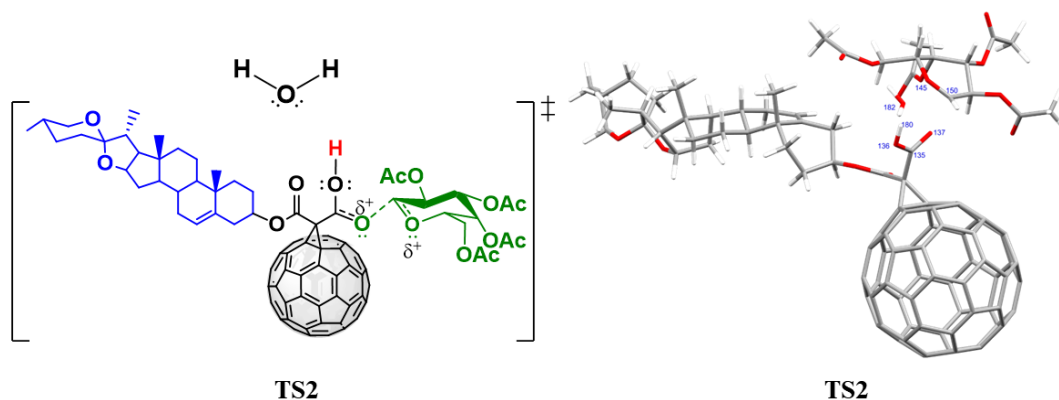
*Figure 38 Predicted **TS2** for step 2 of postulated H_3O^+-assisted Mechanism I related to the concerted release of galactose cation and carboxylic acid formation.*

Finally, the carboxylic acid **3**, the resonance structure that contributes the most to the resonance hybrid of the galactose cation **Gal3** and H_2O are calculated together as hydrolysis products. The optimized final state is shown in Figure 39.
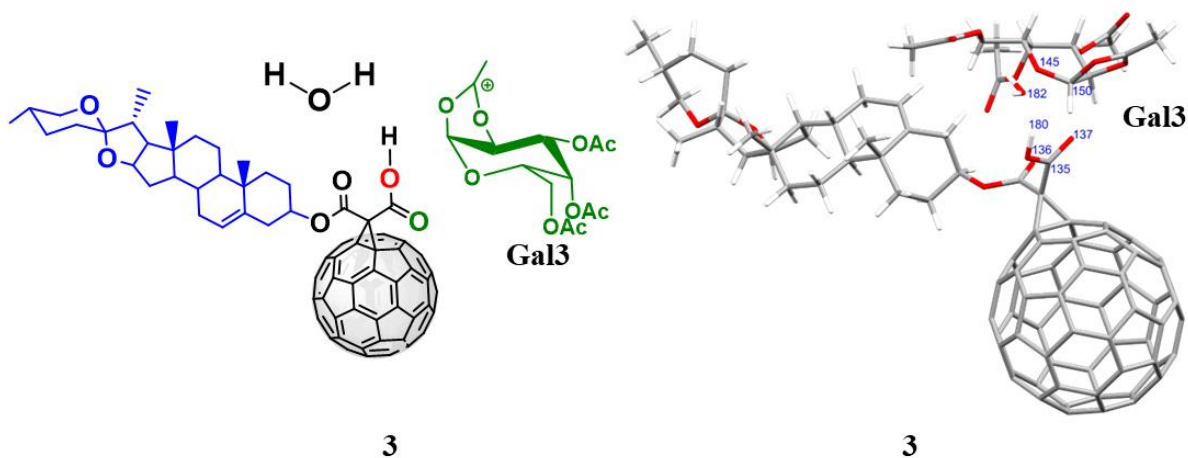
*Figure 39 Predicted hydrolysis products **3**, **Gal3**, and H_2O for the postulated Mechanism I.*

Once the molecular geometries of the structures participating in the H_3O^+ - assisted ester **2** hydrolysis were optimized, the vibrational frequencies of each structure were calculated. The vibrational frequencies for the minimum structures were under -50 cm^{-1} which agrees with the semi-empirical methods. The vibrational frequency determined for the **TS1** was -2429.71, which corresponds to the movement of the atom involved in the protonation step. For the **TS2**, the calculated frequency was -151.61 cm^{-1}, related to the breaking of the ester bond. The most

important atom distances involved in the described H_3O^+-assisted reaction mechanism are represented in Table 10.

Table 10 Distances between the atoms involved in the H_3O^+-assisted hydrolysis of 2

# Atoms	Starting reagents	TS1	INT	TS2	Products
			Distances Å		
182-180	0.995	1.297	1.713	1.775	1.775
180-136	1.703	1.261	0.998	0.969	0.968
136-135	1.225	1.250	1.279	1.314	1.331
135-137	1.352	1.332	1.316	1.249	1.228
137-150	1.419	1.429	1.447	1.937	2.82
150-145	1.408	1.402	1.4	1.297	1.353

The potential energy profile (PEP) for the H_3O^+-assisted hydrolysis of compound **2** was established through calculations in the gas phase using PM3 level of theory and is represented in Figure 40. In contrast to the PEP previously determined for the DBUH⁺-assisted hydrolysis, this process was exothermic (ΔH = -4.49 kcal/mol), it also showed a bimodal PEP. The rate-limiting step was the first one, with a theoretical activation free energy of 9.82 kcal/mol, and the second step comprised a lower activation energy of 8.6 kcal/mol. The calculated relative energies, enthalpies and free energies are summarized in Table 11

Figure 40 Computed potential energy diagram (PED) for H_3O^+-assisted hydrolysis of 2 in gas phase at PM3 level.

	Starting reagents	TS1	INT	TS2	Products
			PM3		
ΔE	0.00	16.65	6.09	15.75	-2.64
ΔH	0.00	11.25	5.53	13.79	-4.49
ΔG	0.00	9.82	3.35	11.95	-5.80

Based on the calculated potential energy profiles shown in Figure 34 and Figure 40, it is possible to propose that the unusual hydrolysis of the Bingel-Hirsch product **2** is due to the presence of hydronium ions. Besides, the neighbor group effect of the acetate group on the C2 of D-galactose moiety contributes to the release of the sugar moiety by stabilizing galactose cation.

3.5.3. Comparison of hydrolysis with $DBUH^+$ and H_3O^+

In principle, the hydrolysis of the Bingel product could be assisted by $DBUH^+$ or H3O$^+$. Theoretically, we have determined that the hydrolysis of compound 2 by $DBUH^+$ is not thermodynamically favored because it is not a spontaneous reaction ($ΔG > 0$). In contrast, hydrolysis assisted by H_3O^+ is thermodynamically favored because it is a spontaneous process ($ΔG < 0$). This stability is achieved because H_2O is a stronger base than DBU; thus, its conjugated acid H_3O^+ can protonate the carbonyl group more easily. Therefore, we can conclude that $DBUH^+$ is a weak acid unable to protonate the molecule to trigger the ester hydrolysis.

The kinetic of the ester hydrolysis determined by the slower step indicates that the first activation free energy ($ΔG$) is higher with $DBUH^+$ than H_3O^+. The calculations show values of $ΔG = 24.20$ kcal/mol and 9.82 kcal/mol, respectively. It means it is more energy demanding to activate **2** to deal with hydrolysis using $DBUH^+$ than H_3O^+. The theoretical result is also supported by the reported basicity of each one. These values support the idea that the $DBUH^+$ is a weak acid unable to cause the ester hydrolysis.

Moreover, the kinetic of this reaction can be improved using some complexes of Co, Pd, and Cu to catalyze the ester hydrolysis[76]. In this way, we can reduce the activation free energies and obtain a faster reaction.

3.5.4. Descarboxylation

After decomposition of compound 2, we obtained compound 3 with the β-ketoacid functional group which is readily decarboxylated at room temperature in acidic solution. Figure 41 represents the decarboxylation mechanism of compound 3. In this way, the Bingel-Hirsch product is decomposed releasing the galactose giving off compound 3 which is easily decarboxylated resulting in compound 4. Finally, we presented a plausible mechanism that explains the decomposition of the Bingel-Hirsch product in acidic medium resulting in the unexpected product.
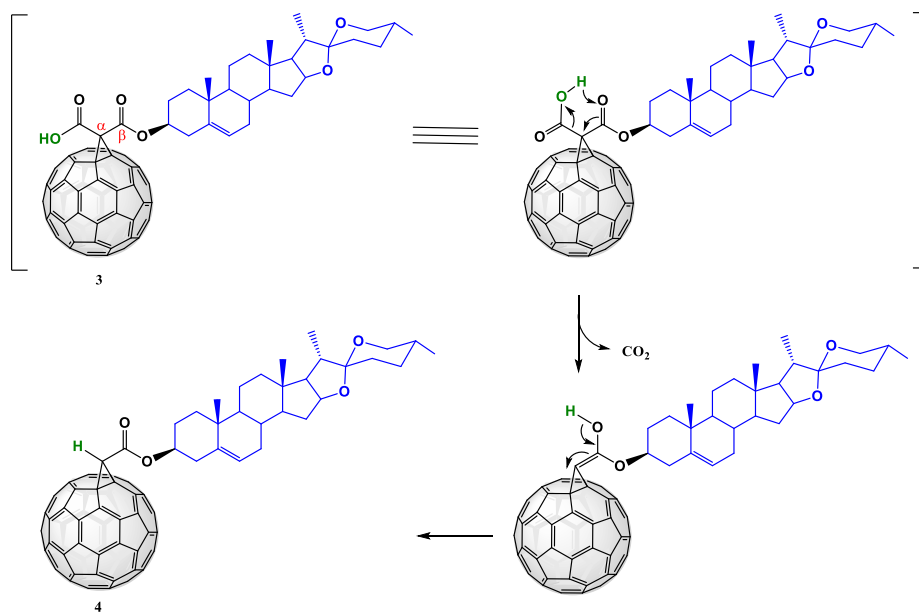
Figure 41 Decarboxylation of compound 3.

4. Conclusions

- Under Bingel-Hirsch's reaction of the D-galactose-diosgenin malonate and fullerene, the expected **2** was not obtained, and the hybrid Diosgenin-C_{60} **4** was isolated and characterized using NMR, FTIR, and MALDI-TOF spectrometry. $DBUH^+$ and H_3O^+ were determined as possibly responsible for the acid-catalyzed hydrolysis of **2**.

- Theoretical calculations were used to support the experimental results. DFT at the PBE/6-31G level of theory was used to optimize the structural geometries of compounds. The most stable conformation for the expected Bingel-Hirsch product **2** was **2C-a,** with the s-trans conformation agreeing with previous reports for similar structures.

- The experimental results made it possible to propose the hydrolysis mechanism as the acid-catalyzed unimolecular alkyl cleavage ($A_{AL}1$). This mechanism is favored by forming a highly stable and excellent leaving group from the galactose release, promoted by delocalization, tertiary carbocation, and five-member ring formation. Moreover, the $A_{AL}1$ mechanism requires low acid concentrations.

- All theoretical physicochemical parameters were consistent with the structures of **2**, and **4** and showed that the hydrolysis and subsequent decarboxylation do not cause drastic changes in the properties analyzed. As expected, **4** has a smaller volume and solvent-accessible surface area (SASA) than **2**. The calculated topological surface area (TPSA) predicted that **4** and **2** could traverse biological membranes. Both compounds showed polarity in the same range which make them more polar than C_{60}, and **4** showed higher $logP_{ow}$, assuming higher hydrophobicity.

- The EPM of compound 4 shows that diosgenin covalently connected to fullerene modified the electrostatic potential distribution indicating the presence of electron rich and poor regions.

- The semi-empirical method at the PM3 level was employed to obtain the Potential Energy Profile (PEP) for the proposed mechanisms. Both $DBUH^+$ and H_3O^+ -assisted hydrolysis mechanisms showed a bimodal profile where the first step was the rate-determining step. According to the optimization energies, it was theoretically demonstrated that the H_3O^+-assisted hydrolysis is thermodynamic and kinetically favored. Moreover, the kinetic analysis showed that free activation energies for the hydrolysis are more energy demanding to overcome with $DBUH^+$ than H_3O^+, which was

related with the weakness of the conjugated acid DBUH$^+$ making it unable to trigger favorable hydrolysis.

5. Recommendations

- DFT calculations should be performed to obtain the Potential Energy Diagram (PED) of the hydrolysis in both the gas phase and implicit solvent, to verify the diagram obtained by the semi-empirical method. Moreover, these calculations will allow more accurate information about the charges and molecular orbitals.

6. References

(1) BeMiller, J. N. Monosaccharides. *Carbohydrate Chemistry for Food Scientists* **2019**, 1–23. https://doi.org/10.1016/B978-0-12-812069-9.00001-7.

(2) Stylianopoulos, C. Carbohydrates: Chemistry and Classification. *Encyclopedia of Human Nutrition* **2012**, *1–4*, 265–271. https://doi.org/10.1016/B978-0-12-375083-9.00041-6.

(3) Conte, F.; van Buuringen, N.; Voermans, N. C.; Lefeber, D. J. Galactose in Human Metabolism, Glycosylation and Congenital Metabolic Diseases: Time for a Closer Look. *Biochimica et Biophysica Acta - General Subjects* **2021**, *1865* (8), 129898. https://doi.org/10.1016/J.BBAGEN.2021.129898.

(4) Bo-Htay, C.; Shwe, T.; Chattipakorn, S. C.; Chattipakorn, N. The Role of D-Galactose in the Aging Heart and Brain. *Molecular Nutrition Carbohydrates* **2019**, 285–301. https://doi.org/10.1016/B978-0-12-849886-6.00022-7.

(5) Escobar-Sánchez, M. L.; Sánchez-Sánchez, L.; Sandoval-Ramírez, J. Steroidal Saponins and Cell Death in Cancer. *Cell Death - Autophagy, Apoptosis and Necrosis* **2015**. https://doi.org/10.5772/61438.

(6) Jesus, M.; Martins, A. P. J.; Gallardo, E.; Silvestre, S. Diosgenin: Recent Highlights on Pharmacology and Analytical Methodology. **2016**. https://doi.org/10.1155/2016/4156293.

(7) Parama, D.; Boruah, M.; Yachna, K.; Rana, V.; Banik, K.; Harsha, C.; Thakur, K. K.; Dutta, U.; Arya, A.; Mao, X.; Ahn, K. S.; Kunnumakkara, A. B. Diosgenin, a Steroidal Saponin, and Its Analogs: Effective Therapies against Different Chronic Diseases. *Life Sciences* **2020**, *260*. https://doi.org/10.1016/J.LFS.2020.118182.

(8) Aguilar, Z. P. Types of Nanomaterials and Corresponding Methods of Synthesis. *Nanomaterials for Medical Applications* **2013**, 50.

(9) Kroto, H. W.; Heath, J. R.; O'Brien, S. C.; Curl, R. F.; Smalley, R. E. C60: Buckminsterfullerene. *Nature* **1985**, *318* (6042), 162–163. https://doi.org/10.1038/318162A0.

(10)   Enes, R. F.; Tomé, A. C.; Cavaleiro, J. A. S.; El-Agamey, A.; McGarvey, D. J. Synthesis and Solvent Dependence of the Photophysical Properties of [60]Fullerene-Sugar Conjugates. *Tetrahedron* **2005**, *61* (50), 11873–11881. https://doi.org/10.1016/j.tet.2005.09.078.

(11)   Fejes, Z.; Hadházi, Á.; Ruth, E.; Csávás, M.; Bereczki, I.; Borbás, A.; Herczegh, P. Synthesis of Ether-Linked [60]Fullerene Glycoconjugates by Nucleophilic Cyclopropanation. *Chemical Papers* **2015**, *69* (6), 896–900. https://doi.org/10.1515/chempap-2015-0087.

(12)   Almagro, L.; Lemos, R.; Makowski, K.; Rodríguez, H.; Ortiz, O.; Cáceres, W.; Herranz, M. Á.; Molero, D.; Martínez-Álvarez, R.; Suárez, M.; Martín, N. [60]Fullerene Hybrids Bearing "Steroid Wings": A Joined Experimental and Theoretical Investigation. *European Journal of Organic Chemistry* **2020**, *2020* (37), 5926–5937. https://doi.org/10.1002/EJOC.202000989.

(13)   Goodarzi, S.; da Ros, T.; Conde, J.; Sefat, F.; Mozafari, M. Fullerene: Biomedical Engineers Get to Revisit an Old Friend. *Materials Today* **2017**, *20* (8), 460–480. https://doi.org/10.1016/J.MATTOD.2017.03.017.

(14)   Prato, M. [60]Fullerene Chemistry for Materials Science Applications. *Journal of Materials Chemistry* **1997**, *7* (7), 1097–1109. https://doi.org/10.1039/A700080D.

(15)   Bakry, R.; Vallant, R. M.; Najam-Ul-Haq, M.; Rainer, M.; Szabo, Z.; Huck, C. W.; Bonn, G. K. Medicinal Applications of Fullerenes. *International Journal of Nanomedicine* **2007**, *2* (4), 639–649.

(16)   Fagan, P. J.; Calabrase, J. C.; Malone, B. Metal Complexes of Buckminsterfullerene (C60). *Accounts of Chemical Research* **1992**, *25* (3), 134–142.

(17)   Dinadayalane, T.; Leszczynski, J. Fundamental Structural, Electronic, and Chemical Properties of Carbon Nanostructures: Graphene, Fullerenes, Carbon Nanotubes, and Their Derivatives. In *Handbook of Computational Chemistry*; Leszczynski, J., Ed.; Springer Netherlands: Mississipi; pp 793–867.

(18)   Park, S.; Srivastava, D.; Cho, K. External Chemical Reactivity of Fullerenes and Nanotubes. MRS Proceedings, 675 |. *Materials Research Society* **2001**, *675*.

(19)   Guimarães Pedrosa, M. C.; Dutra Filho, J. C.; Rodrigues de Menezes, L.; Oliveira da Silva, E. Chemical Surface Modification and Characterization of Carbon Nanostructures Without Shape Damage. *Materials Research* **2020**, 8. https://doi.org/10.1590/1980-5373-MR-2019-0493.

(20)   Thakral, S.; Mehta, R. Fullerenes: An Introduction and Overview of Their Biological Properties. *Indian Journal of Pharmaceutical Sciences* **2006**, *68* (1), 13. https://doi.org/10.4103/0250-474X.22957.

(21)   Narumi, A.; Nakazawa, T.; Shinohara, K.; Kato, H.; Iwaki, Y.; Okimoto, H.; Kikuchi, M.; Kawaguchi, S.; Hino, S.; Ikeda, A.; Shaykoon, M. S. A.; Shen, X.; Duan, Q.; Kakuchi, T.; Yasuhara, K.; Nomoto, A.; Mikata, Y.; Yano, S. C60 Fullerene with Tetraethylene Glycols as a Well-Defined Soluble Building Block and Saccharide-Conjugation Producing PDT Photosensitizer. *Chemistry Letters* **2019**, *48* (10), 1209–1211. https://doi.org/10.1246/CL.190492.

(22)   Nierengarten, I.; Nierengarten, J.-F. Fullerene Sugar Balls: A New Class of Biologically Active Fullerene Derivatives FOCUS REVIEW. *Chem. Asian J* **2014**, *00*, 0–0. https://doi.org/10.1002/asia.201400133.

(23)   Alonso, D.; Hernández-Castillo David; Almagro, L.; Gonzáles, A. R.; Hernández-Castillo, D.; Almagro, L.; González-Alemán, R.; Molero, D.; Herranz, M. A.; Medina-Páez, E.; Coro, J.; Martínez-Álvarez, R.; Suárez, M.; Martín, N. Diastereoselective Synthesis of Steroid-[60]Fullerene Hybrids and Theoretical Underpinning. The Journal of Organic Chemistry | 10.1021/Acs.Joc.9b03121. *The Journal of Organic Chemistry* **2020**, *85*, 2426–2437.

(24)   Tanimoto, S.; Takahashi, D.; Toshima, K. Chemical Methods for Degradation of Target Proteins Using Designed Light-Activatable Organic Molecules. *Chemical Communications* **2012**, *48* (62), 7659–7671. https://doi.org/10.1039/C2CC30831B.

(25) Mroz, P.; Tegos, G. P.; Gali, H.; Wharton, T.; Sarna, T.; Hamblin, M. R. Photodynamic Therapy with Fullerenes. *Photochemical and Photobiological Sciences* **2007**, *6* (11), 1139–1149. https://doi.org/10.1039/B711141J.

(26) Fouejio, D.; Yossa Kamsi, R. A.; Tadjouteu Assatse, Y.; Ejuh, G. W.; Ndjaka, J. M. B. DFT Studies of the Structural, Chemical Descriptors and Nonlinear Optical Properties of the Drug Dihydroartemisinin Functionalized on C60 Fullerene. *Computational and Theoretical Chemistry* **2021**, *1202*. https://doi.org/10.1016/J.COMPTC.2021.113298.

(27) MITCHELL, I.; SUBBIAH, A.; BENSIMON, D. D. LIPOFULLERENE-SACCHARIDE CONJUGATES AND THEIR USE AS ANTIMETASTATIC AGENTS FOR THE INHIBITION OF MAMMALIAN NEOPLASMS. WO2018156923, 2018.

(28) Liu, H.; Guo, Y.; Wang, X.; Liang, X.; Liu, X.; Jiang, S. A Novel Fullerene Oxide Functionalized Silica Composite as Stationary Phase for High-Performance Liquid Chromatography. *RSC Advances* **2014**, *4* (34), 17541–17548. https://doi.org/10.1039/C4RA01408A.

(29) dos Santos, L. J.; Rocha, G. P.; Alves, R. B.; de Freitas, R. P. Fullerene C60: Chemistry and Applications. *Quimica Nova* **2010**, *33* (3), 680–693. https://doi.org/10.1590/S0100-40422010000300036.

(30) Darwish, A. D. Fullerenes. *Annual Reports on the Progress of Chemistry - Section A* **2013**, *109*, 436–452. https://doi.org/10.1039/C3IC90012F.

(31) Rasovic, I. Water-Soluble Fullerenes for Medical Applications. *Materials Science and Technology* **2017**. https://doi.org/10.1080/O2670836.2016.1198114.

(32) Bingel, C. Cyclopropanierung von Fullerenen. *Chem Ber* **1993**, *126* (8), 1957–1959. https://doi.org/10.1002/CBER.19931260829.

(33) Hirsch, A.; Lamparth, I.; Grösser, T.; Karfunkel, H. R. Regiochemistry of Multiple Additions to the Fullerene Core: Synthesis of a Tb-Symmetric Hexakisadduct of

C60 with Bis(Ethoxycarbonyl)Methylene. *J Am Chem Soc* **1994**, *116* (20), 9385–9386. https://doi.org/10.1021/JA00099A088.

(34)   Piotrowski, P.; Pawłowska, J.; Pawłowski, J.; Więckowska, A.; Bilewicz, R.; Kaim, A. Nanostructured Films of in Situ Deprotected Thioacetyl-Functionalized C60-Fullerenes on a Gold Surface. *Journal of Materials Chemistry A* **2014**, *2* (7), 2353–2362. https://doi.org/10.1039/C3TA13844E.

(35)   Camps, X.; Hirsch, A. Efficient Cyclopropanation of C60 Starting from Malonates. *Journal of the Chemical Society - Perkin Transactions 1* **1997**, No. 11, 1595–1596. https://doi.org/10.1039/A702055D.

(36)   Carey, F. A.; Sundberg, R. J. Addition, Condensation and Substitution Reactions of Carbonyl Compounds. *Advanced Organic Chemistry* **2007**, 629–711. https://doi.org/10.1007/978-0-387-44899-2_7.

(37)   Gómez-Bombarelli, R.; Calle, E.; Casado, J. Mechanisms of Lactone Hydrolysis in Acidic Conditions. *Journal of Organic Chemistry* **2013**, *78* (14), 6880–6889. https://doi.org/10.1021/JO4002596.

(38)   Wang, Z.; Ma, H. Mechanisms of a Cyclobutane-fused Lactone Hydrolysis in Alkaline and Acidic Conditions. *Molecules* **2021**, *26* (12). https://doi.org/10.3390/MOLECULES26123519.

(39)   Smith, M. B.; March, J. Addition to Carbon–Hetero Multiple Bonds. In *MARCH'S ADVANCED ORGANIC CHEMISTRY REACTIONS*; John Wiley & Sons, Inc: USA, 2007; pp 1402–1407.

(40)   Doi, K.; Togano, E.; Xantheas, S. S.; Nakanishi, R.; Nagata, T.; Ebata, T.; Inokuchi, Y. Microhydration Effects on the Intermediates of the SN2 Reaction of Iodide Anion with Methyl Iodide. *Angewandte Chemie - International Edition* **2013**, *52* (16), 4380–4383. https://doi.org/10.1002/ANIE.201207697.

(41)   He, L.; Bai, L.; Dionysiou, D. D.; Wei, Z.; Spinney, R.; Chu, C.; Lin, Z.; Xiao, R. Applications of Computational Chemistry, Artificial Intelligence, and Machine

Learning in Aquatic Chemistry Research. *Chemical Engineering Journal* **2021**, *426*, 131810. https://doi.org/10.1016/J.CEJ.2021.131810.

(42) Singh, S.; Bani Baker, Q.; Singh, D. B. Molecular Docking and Molecular Dynamics Simulation. *Bioinformatics* **2022**, 291–304. https://doi.org/10.1016/B978-0-323-89775-4.00014-6.

(43) Adcock, S. A.; McCammon, J. A. Molecular Dynamics: Survey of Methods for Simulating the Activity of Proteins. *Chemical Reviews* **2006**, *106* (5), 1589–1615. https://doi.org/10.1021/cr040426m.

(44) Thiel, W. Semiempirical Quantum–Chemical Methods. *WIREs Computational Molecular Science* **2014**, *4* (2), 145–157. https://doi.org/10.1002/wcms.1161.

(45) Ramachandran, K. I.; Gopakumar, D.; Namboor, K. *Computational Chemistry and Molecular Modeling* ; Springer, Berlin, Heidelberg, 2008.

(46) Jensen, F. *Introduction to Computational Chemistry*, Second.; John Wiley & Sons Ltd: West Sussex, 2007.

(47) Perdew, J. P.; Ruzsinszky, A.; Tao, J.; Staroverov, V. N.; Scuseria, G. E.; Csonka, G. I. Prescription for the Design and Selection of Density Functional Approximations: More Constraint Satisfaction with Fewer Fits. *The Journal of Chemical Physics* **2005**, *123* (6), 062201. https://doi.org/10.1063/1.1904565.

(48) Ying Zhang, I.; Xu, X. On the Top Rung of Jacob's Ladder of Density Functional Theory: Toward Resolving the Dilemma of SIE and NCE. *WIREs Comput Mol Sci* **2021**, 11. https://doi.org/10.1002/wcms.1490.

(49) Frank Jensen. *Introduction to Computational Chemistry*, 2nd ed.; John Wiley & Sons Ltd: West Sussex PO19 8SQ, England, 2007.

(50) Jensen, F. Polarization Consistent Basis Sets: Principles. *Journal of Chemical Physics* **2001**, *115* (20), 9113–9125. https://doi.org/10.1063/1.1413524.

(51) Wennmohs, F.; Aravena, D.; Atanasov, M.; Becker, U.; Bykov, D.; Chilkuri, V. G.; Datta, D.; Dutta, A. K.; Ganyushin, D.; Guo, Y.; Hansen, A.; Huntington, L.; Izsák,

R.; Kollmar, C.; Kossmann, S.; Krupička, M.; Lenk, D.; Liakos, D. G.; Manganas, D.; Pantazis, D. A.; Petrenko, T.; Pinski, P.; Reimann, C.; Retegan, M.; Riplinger, C.; Risthaus, T.; Roemelt, M.; Saitow, M.; Sandhöfer, B.; Schapiro, I.; Sivalingam, K.; Stoychev, G.; Wezisla, B.; Kállay, M.; Grimme, S.; Valeev, E.; Chan, G.; Pittner, J.; Brehm, M.; Bistoni, G.; Schneider, W.; Lehnhausen, S. Orca Manual. **2017**, 827.

(52)   Tosoni, S.; Tuma, C.; Sauer, J.; Civalleri, B.; Ugliengo, P. A Comparison between Plane Wave and Gaussian-Type Orbital Basis Sets for Hydrogen Bonded Systems: Formic Acid as a Test Case. *Journal of Chemical Physics* **2007**, *127* (15), 154102. https://doi.org/10.1063/1.2790019.

(53)   Kantorovich, L. *Quantum Theory of the Solid State: An Introduction*; Springer Netherlands, 2004. https://doi.org/10.1007/978-1-4020-2154-1.

(54)   Kjær, H.; Sauer, S. P. A. Pople Style Basis Sets for the Calculation of NMR Spin-Spin Coupling Constants: The 6-31G-J and 6-311G-J Basis Sets. *Journal of Chemical Theory and Computation* **2011**, *7* (12), 4070–4076. https://doi.org/10.1021/CT200546Q.

(55)   *Microwave-assisted synthesis :: Anton Paar Wiki*. https://wiki.anton-paar.com/en/microwave-assisted-synthesis/ (accessed 2021-05-30).

(56)   Christy, P. A.; Peter, A. J.; Lee, C. W.; Lee, C. W. Structural, Vibrational, Spectroscopic, NMR and Quantum Chemical Studies on Fullerene and Bromofullerenes. *Physica B: Physics of Condensed Matter* **2018**. https://doi.org/10.1016/j.physb.2018.11.038.

(57)   Sattarova, A. F.; Biglova, Y. N.; Mustafin, A. G. Quantum-chemical Approaches in the Study of Fullerene and Its Derivatives by the Example of the Most Typical Cycloaddition Reactions: A Review. *International Journal of Quantum Chemistry* **2021**. https://doi.org/10.1002/qua.26863.

(58) Schlegel, H. B. Geometry Optimization. *Wiley Interdisciplinary Reviews: Computational Molecular Science* **2011**, *1* (5), 790–809. https://doi.org/10.1002/WCMS.34.

(59) Sholl, D. S.; Steckel, J. A. DFT Calculations of Vibrational Frequencies. *Density Functional Theory* **2009**, 113–130. https://doi.org/10.1002/9780470447710.CH5.

(60) Neese, F. Software Update: The ORCA Program System, Version 4.0. *Wiley Interdisciplinary Reviews: Computational Molecular Science* **2017**, *8* (e1327). https://doi.org/10.1002/wcms.1327.

(61) Tang, Z. *Zeyuan Tang's Wiki*. http://wiki.tangzeyuan.com/ (accessed 2022-06-26).

(62) Lemos, R.; Suarez, M. Design of Novel Carbohydrate-Steroid[60]Fullerene Hybrids. Synthesis, Characterization and Theoretical Studies. PhD Thesis in progress, University of Havana, Havana, 2022.

(63) Suárez, M.; Makowski, K.; Lemos, R.; Almagro, L.; Rodríguez, H.; Herranz, M. Á.; Molero, D.; Ortiz, O.; Maroto, E.; Albericio, F.; Murata, Y.; Martín, N. An Androsterone-H2@C60 Hybrid: Synthesis, Properties and Molecular Docking Simulations with SARS-Cov-2. *Chempluschem* **2021**, *86* (7), 972–981. https://doi.org/10.1002/CPLU.202000770.

(64) Almagro, L.; Hernández-Castillo, D.; Ortiz, O.; Alonso, D.; Ruiz, A.; Coro, J.; Herranz, M. Á.; Molero, D.; Martínez-Álvarez, R.; Suárez, M.; Martín, N. Steroid–Fullerene Hybrids from Epiandrosterone: Synthesis, Characterization and Theoretical Study. *European Journal of Organic Chemistry* **2018**, *2018* (33), 4512–4522. https://doi.org/10.1002/EJOC.201800622.

(65) Schaeffer, L. The Role of Functional Groups in Drug-Receptor Interactions. *The Practice of Medicinal Chemistry: Fourth Edition* **2008**, 359–378. https://doi.org/10.1016/B978-0-12-417205-0.00014-6.

(66) Durham, E.; Dorr, B.; Woetzel, N.; Staritzbichler, R.; Meiler, J. Solvent Accessible Surface Area Approximations for Rapid and Accurate Protein Structure Prediction.

Journal of Molecular Modeling **2009**, *15* (9), 1093–1108. https://doi.org/10.1007/S00894-009-0454-9.

(67) Mitternacht, S.; Hubbard, S. J.; Zhou, Y. FreeSASA: An Open Source C Library for Solvent Accessible Surface Area Calculations [Version 1; Peer Review: 2 Approved]. **2016**. https://doi.org/10.12688/f1000research.7931.1.

(68) Masuda, T.; Jikihara, T.; Nakamura, K.; Kimura, A.; Takagi, T.; Fujiwara, H. Introduction of Solvent-Accessible Surface Area in the Calculation of the Hydrophobicity Parameter Log P from an Atomistic Approach. *Journal of Pharmaceutical Sciences* **1997**, *86* (1), 57–63. https://doi.org/10.1021/JS960237M.

(69) Palm, K.; Stenberg, P.; Luthman, K.; Artursson, P. Polar Molecular Surface Properties Predict the Intestinal Absorption of Drugs in Humans. *Pharm Res* **1997**, *14* (5), 568–571. https://doi.org/10.1023/A:1012188625088.

(70) Bader, R. F. W.; Larouche, A.; Gatti, C.; Carroll, M. T.; MacDougall, P. J.; Wiberg, K. B. Properties of Atoms in Molecules: Dipole Moments and Transferability of Properties. *The Journal of Chemical Physics* **1998**, *87* (2), 1142. https://doi.org/10.1063/1.453294.

(71) Antoine, R.; Dugourd, P.; Rayane, D.; Benichou, E.; Broyer, M.; Chandezon, F.; Guet, C. Direct Measurement of the Electric Polarizability of Isolated C60 Molecules. *Journal of Chemical Physics* **1999**, *110* (19), 9771–9772. https://doi.org/10.1063/1.478944.

(72) Hossein Fekri, M.; Bazvand, R.; Soleymani, M.; Razavi Mehr, M. Adsorption of Metronidazole Drug on the Surface of Nano Fullerene C60 Doped with Si, B and Al: A DFT Study. *International Journal of Nano Dimension* **2020**, 346–354.

(73) Kakkar, R.; Sarma, B. K.; Katoch, V. Theoretical Study of the Mechanism of Proton Transfer in Tautomeric Systems: Alloxan. *Journal of Chemical Sciences* **2001**, *113* (4), 297–306.

(74) Fatollahpour, M.; Tahermansouri, H. DFT Study of the Intramolecular Double Proton Transfer of 2,5-Diamino-1,4-Benzoquinone and Its Derivatives, and

Investigations about Their Aromaticity. *Comptes Rendus Chimie* **2017**, *20* (9–10), 942–951. https://doi.org/10.1016/j.crci.2017.06.001.

(75) Hori, K.; Ikenaga, Y.; Arata, K.; Takahashi, T.; Kasai, K.; Noguchi, Y.; Sumimoto, M.; Yamamoto, H. Theoretical Study on the Reaction Mechanism for the Hydrolysis of Esters and Amides under Acidic Conditions. *Tetrahedron* **2007**, *63* (5), 1264–1269. https://doi.org/10.1016/J.TET.2006.11.039.

(76) Tokunaga, M.; Aoyama, H.; Kiyosu, J.; Shirogane, Y.; Iwasawa, T.; Obora, Y.; Tsuji, Y. Metal Complexes-Catalyzed Hydrolysis and Alcoholysis of Organic Substrates and Their Application to Kinetic Resolution. *Journal of Organometallic Chemistry* **2007**, *692* (1–3), 472–480. https://doi.org/10.1016/j.jorganchem.2006.06.045.